

Flexocurrent-induced magnetization: Strain gradient-induced magnetization in time-reversal symmetric systems

Shinnosuke Koyama,¹ Takashi Koretsune,² and Kazumasa Hattori¹

¹*Department of Physics, Tokyo Metropolitan University,
1-1, Minami-osawa, Hachioji, Tokyo 192-0397, Japan*

²*Department of Physics, Tohoku University, Sendai, Miyagi 980-8578, Japan*
(Dated: February 5, 2026)

Symmetry constraints determine which physical responses are allowed in a given system. Magnetization induced by strain fields—such as in piezomagnetic and flexomagnetic effects—has typically been considered in materials that break time-reversal symmetry. Here, we propose that nonuniform strain can induce magnetization even in nonmagnetic metals and semiconductors that preserve time-reversal symmetry. This mechanism differs from the conventional flexomagnetic effect: the strain gradient acts as a driving force on the electrons, generating magnetization in a manner closely analogous to current-induced magnetization. Treating the strain field as an external field, we derive a general expression for the magnetization induced by a strain gradient and demonstrate that this response is symmetry-allowed even in time-reversal symmetric systems. We apply our formulation to nonmagnetic systems that lack spatial inversion symmetry while preserving time-reversal symmetry, using a decorated square lattice, monolayer MoS₂, and monolayer Janus MoSSe as representative examples. We find a finite magnetization response to strain gradients, which is consistent with symmetry arguments, supporting the validity of our theoretical framework. These results offer a pathway for controlling magnetization in nonmagnetic materials using strain fields.

I. INTRODUCTION

In condensed matter physics, cross-correlation responses—where the symmetry of an observable differs from that of the applied external field—have attracted significant attention [1] since the discovery of the magnetoelectric effect in Cr₂O₃ [2]. These responses emerge in systems with symmetry breaking fields such as the spatial distribution of spins [3, 4], electric dipoles [5, 6], and various multipole moments [7, 8]. They are group-theoretically classified by their macroscopic symmetry under the symmetry broken phases. Once the macroscopic symmetry is identified, which cross correlations emerge can be readily obtained [9]. To systematically carry out them, a multipolar expansion of local and cluster degrees of freedom is powerful and provides a unified description of the couplings between different degrees of freedom [10–13].

The cross-correlation responses are of fundamental importance because they directly reflect symmetry breaking and, at the same time, offer considerable potential for device applications [14–20]. In particular, cross-correlated phenomena enable the interconversion among electric, magnetic, and mechanical signals, forming the basis of many spintronic and multiferroic applications. Among these, the control of magnetization is a central issue in spintronics, motivating extensive efforts toward low-power, high-density magnetic manipulation using nonconjugate external fields [18, 19]. Representative examples of magnetization responses driven by nonconjugate fields include the magnetoelectric effect [5, 21–24] and the piezomagnetic effect [11, 25]. Since these responses are induced by external fields whose transformation under time reversal differs from that of magnetization, they can occur only in systems with broken time-reversal symmetry (TRS) [10, 11]. As a result, most studies have focused on magnetic materials.

The magnetoelectric and piezomagnetic effects are equilib-

rium magnetization responses, and whether such responses are allowed is strictly determined by the symmetry of the system. For nonequilibrium responses, however, the conditions imposed by TRS are modified. A representative example is current-induced magnetization (CIM) in metals, also known as the Edelstein effect [26–28]. CIM arises in systems that exhibit spin-momentum locking in their electronic band structures, irrespective of whether the underlying symmetry-breaking fields are magnetic or nonmagnetic. When an external electric field is applied, it acts as a driving force on the electrons and generates a nonequilibrium modification in their distribution function. In the presence of dissipation—due to, for example, impurity scattering—the system relaxes into a nonequilibrium steady state that carries a finite electric current, which effectively breaks TRS. This nonequilibrium distribution then gives rise to a finite magnetization through spin-momentum locking. Since CIM is a symmetry-allowed response even in systems that preserve TRS, it provides a powerful route to generate and control spin polarization and spin currents in nonmagnetic materials [29].

Recently, increasing attention has been directed toward magnetization induced by strain gradients. This phenomenon, known as the flexomagnetic effect, is defined as the equilibrium linear response of magnetization to a strain gradient [30–32]. In nanoscale materials, thin films, and nanowires, large strain gradients can naturally arise [33], thereby significantly enhancing the response. As a result, small devices can generate substantial strain gradients with minimal deformation, enabling functionalities beyond those achievable with conventional magnetic devices [34]. Because strain gradients are rank-3 tensors, they can induce nonzero magnetization responses in a broad range of magnetic point groups [35]. Theoretically, strain gradient-induced magnetization has been predicted in various materials, including Mn₃GaN [31], VSe₂ [36], CrI₃ [37–39], FeSe [40], CoTe [41], and Mn-doped MoS₂ [42]. Experimentally, the flexomag-

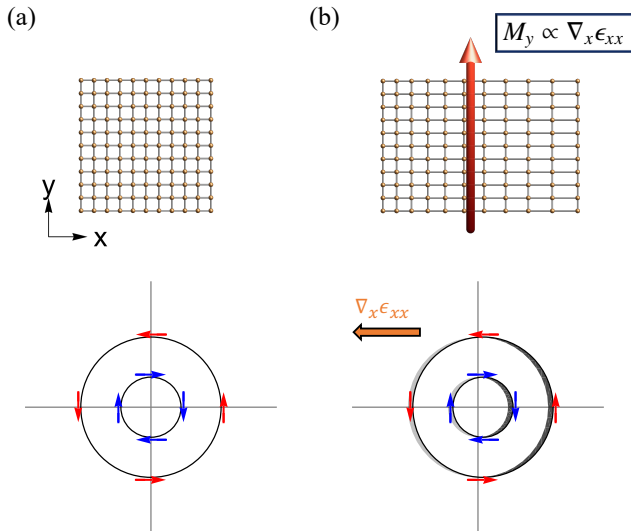


FIG. 1. Schematic illustration of the flexocurrent-induced magnetization under $\nabla_x \epsilon_{xx}$. (a) A system exhibiting Rashba spin-momentum locking in the absence of external strain. (b) In the presence of a strain field with a finite strain gradient $\nabla_x \epsilon_{xx}$, the strain gradient acts as a driving force. With momentum relaxation due to scattering mechanisms such as impurity scattering, a nonequilibrium steady state with an asymmetric distribution is sustained, resulting in a finite magnetization. The shaded regions indicate asymmetric distribution of electrons in momentum space due to the strain gradient.

netic effect has been observed in alloy films [43, 44] and in Cr_2O_3 [45], highlighting its potential for magnetization control via strain gradients.

In equilibrium, magnetization responses induced by strain fields—such as the piezomagnetic and flexomagnetic effects—are generally restricted to systems that break TRS. This restriction arises because both strain and its spatial gradient are even under time reversal, whereas magnetization is odd. However, when nonequilibrium responses are considered, a finite magnetization can emerge even in systems that preserve TRS. Since strain can couple to electric quadrupoles [46–49], a spatially varying strain generates a coupling term in the equations of motion and acts as a driving force on the electrons. In the presence of dissipation, this driving force leads to a nonequilibrium steady state characterized by an asymmetric electronic distribution. This nonequilibrium state effectively breaks TRS and can induce finite magnetization. This mechanism serves as a mechanical analog of CIM and suggests a novel route for controlling magnetization using strain fields in nonmagnetic materials.

In this study, we formulate the magnetization response driven by a strain gradient in time-reversal symmetric systems without magnetic orders. Starting from a simple free-fermion Hamiltonian with orbital (electric quadrupole) degrees of freedom, we introduce strain fields that couple to the electric quadrupoles. Employing Luttinger’s method [50], we derive a Kubo formula [51] for the magnetization induced by a strain gradient. This response is nonequilibrium in na-

ture and should be distinguished from the flexomagnetic effect. We refer to this magnetization response as flexocurrent-induced magnetization (FCIM), where the term flexocurrent denotes the electric-quadrupole current driven by a strain gradient. We apply our formalism to three representative systems: a nonmagnetic two-dimensional square lattice with the C_{4v} point group, a monolayer MoS_2 with the D_{3h} point group, and a monolayer Janus MoSSe with the C_{3v} point group. For all three systems, we evaluate both the atomic orbital and spin components of FCIM. Our results demonstrate that even in nonmagnetic systems with TRS, a finite magnetization can be induced by a strain gradient in the presence of spin-momentum locking. We also perform a simple symmetry analysis to identify the conditions for realizing a finite FCIM, which supports our numerical findings.

This paper is organized as follows. In Sec. II, we review the theoretical framework for FCIM. Section II A introduces a free-fermionic system that serves as an unperturbed Hamiltonian, and Sec. II B introduces a perturbative Hamiltonian in which external strains and the electric quadrupole moments are coupled with each other. Section II C demonstrates, using semiclassical theory, that a strain gradient accelerates electrons and acts as a driving force. In Sec. II D, we give a derivation of the Kubo formula for FCIM. We then provide its symmetry analysis in Sec. II E. In Sec. III, we present numerical results of FCIM in time-reversal symmetric nonmagnetic systems: a two-dimensional square lattice with C_{4v} symmetry (Sec. III A), a monolayer MoS_2 with D_{3h} symmetry (Sec. III B), and a monolayer MoSSe with C_{3v} symmetry (Sec. III C). In Sec. IV, we discuss the future perspectives in both experimental and theoretical points of view. Finally, Sec. V summarizes the main conclusions.

II. THEORY

A. Free-fermion Hamiltonian

We first introduce a free-fermion Hamiltonian, defined as

$$\mathcal{H} = \int d\mathbf{r} \Psi^\dagger(\mathbf{r}) \hat{H} \Psi(\mathbf{r}), \quad (1)$$

where \hat{H} is an $N \times N$ Hermitian matrix and N denotes the number of bands. The field operators $\Psi^\dagger(\mathbf{r})$ and $\Psi(\mathbf{r})$ are N -component vectors constructed from the fermion creation and annihilation operators satisfying the following relation: $\{\Psi_s^\dagger(\mathbf{r}), \Psi_{s'}^\dagger(\mathbf{r}')\} = \delta(\mathbf{r} - \mathbf{r}') \delta_{ss'}$. We introduce the Fourier transform as

$$\Psi_s(\mathbf{r}) = \frac{1}{\sqrt{V}} \sum_{\mathbf{k}} \Psi_{\mathbf{k},s} e^{i\mathbf{k}\cdot\mathbf{r}}, \quad (2)$$

where V denotes the volume of the system and \mathbf{k} is the wave vector. Substituting Eq. (2) into Eq. (1), we obtain

$$\mathcal{H} = \sum_{\mathbf{k}} \Psi_{\mathbf{k}}^\dagger \hat{H}_{\mathbf{k}} \Psi_{\mathbf{k}}, \quad (3)$$

where $\hat{H}_k = e^{-ik\cdot r} \hat{H} e^{ik\cdot r}$ is the Bloch Hamiltonian for the wave vector \mathbf{k} . Introducing an $N \times N$ unitary matrix U_k that diagonalizes \hat{H}_k , Eq. (3) can be rewritten as

$$\mathcal{H} = \sum_k \Gamma_k^\dagger \mathcal{E}_k \Gamma_k, \quad (4)$$

where $\mathcal{E}_k = U_k^\dagger \hat{H}_k U_k = \text{diag}(\varepsilon_{k,1}, \varepsilon_{k,2}, \dots, \varepsilon_{k,N})$, and Γ_k^\dagger is defined as $\Gamma_k^\dagger = \Psi_k^\dagger U_k^\dagger$.

B. Strain fields

We introduce an external strain field. Throughout this section, we assume that the system has cubic point group symmetry. We omit the discussion for other cases such as hexagonal symmetries, since the derivation is straightforward by similar analyses to those shown below.

The strain tensor $\varepsilon(\mathbf{r})$ is a rank-2 symmetric tensor defined as

$$\varepsilon(\mathbf{r}) \equiv \begin{pmatrix} \varepsilon_{xx}(\mathbf{r}) & \varepsilon_{xy}(\mathbf{r}) & \varepsilon_{xz}(\mathbf{r}) \\ \varepsilon_{xy}(\mathbf{r}) & \varepsilon_{yy}(\mathbf{r}) & \varepsilon_{yz}(\mathbf{r}) \\ \varepsilon_{xz}(\mathbf{r}) & \varepsilon_{yz}(\mathbf{r}) & \varepsilon_{zz}(\mathbf{r}) \end{pmatrix}. \quad (5)$$

Since these tensor components generally do not form the cubic irreducible representations, it is useful to rewrite them in the following form:

$$\varepsilon_{x^2-y^2}(\mathbf{r}) = \varepsilon_{xx}(\mathbf{r}) - \varepsilon_{yy}(\mathbf{r}), \quad (6)$$

$$\varepsilon_{3z^2-r^2}(\mathbf{r}) = \frac{1}{\sqrt{3}}[2\varepsilon_{zz}(\mathbf{r}) - \varepsilon_{xx}(\mathbf{r}) - \varepsilon_{yy}(\mathbf{r})], \quad (7)$$

together with $\varepsilon_{xy}(\mathbf{r})$, $\varepsilon_{yz}(\mathbf{r})$, and $\varepsilon_{xz}(\mathbf{r})$. Because the strain tensor is even under both spatial inversion and time reversal, it couples to the electric quadrupole operators $Q_\lambda(\mathbf{r})$ as [46, 47]

$$\mathcal{V} = \sum_\lambda^{\text{Irrep.}} g_\lambda \int d\mathbf{r} \varepsilon_\lambda(\mathbf{r}) Q_\lambda(\mathbf{r}), \quad (8)$$

where $\lambda = \{xy, yz, xz, x^2 - y^2, 3z^2 - r^2\}$, g_λ is the coupling constant between $\varepsilon_\lambda(\mathbf{r})$ and $Q_\lambda(\mathbf{r})$, and $Q_\lambda(\mathbf{r})$ denotes the electric quadrupole density expressed as

$$Q_\lambda(\mathbf{r}) = \frac{1}{2}[\Psi^\dagger(\mathbf{r}) \hat{Q}_\lambda \Psi(\mathbf{r}) + \text{H.c.}], \quad (9)$$

with $\hat{Q}_\lambda = \hat{Q}_\lambda^\dagger$ [52]. Each component of \hat{Q}_λ is defined similarly to that of ε_λ and acts on the local orbital subspace of the electron field $\Psi(\mathbf{r})$. Here, for simplicity, we assume that the couplings between $\varepsilon(\mathbf{r})$ and $Q(\mathbf{r})$ are local in this paper, while it is also possible to derive similar results by taking into account coupling constants between nonlocal orbital degrees of freedom, i.e., hopping between neighboring sites and $\varepsilon(\mathbf{r})$ [53, 54]. Since the isotropic strain component $\varepsilon_{r^2} = \frac{1}{\sqrt{3}}(\varepsilon_{xx} + \varepsilon_{yy} + \varepsilon_{zz})$ necessarily belongs to the trivial representation and transforms as a rank-0 scalar, the coupling in $\lambda = r^2 = x^2 + y^2 + z^2$ is absent in Eq. (8). Consequently, the multipole that couples to ε_{r^2} is not an electric quadrupole but

an electric monopole. From the viewpoint of symmetry, this coupling merely amounts to expressing a scalar potential in terms of the strain field. Accordingly, the physics generated by the coupling term of $\lambda = r^2$ is essentially identical to that arising from the coupling between a scalar potential and an electric monopole. For this reason, we exclude this contribution in the present study.

C. Strain gradient as a driving force

Before formulating magnetization responses to a strain gradient $\nabla \varepsilon_\lambda$, we clarify that $\nabla \varepsilon_\lambda$ acts as a driving force on electrons within the semiclassical theory, and that FCIM is determined by the dissipative part of the nonequilibrium magnetization response tensor.

The eigenvalue equation of \hat{H}_k is given by

$$\hat{H}_k |u_{k,n}\rangle = \varepsilon_{k,n} |u_{k,n}\rangle, \quad (10)$$

where $|u_{k,n}\rangle$ is the Bloch state corresponding to the n th column of U_k and one should regard \hat{H}_k as acting on the Bloch states represented in the bra-ket formalism rather than on the operator Ψ_k in Eq. (3). Using this notation, we define a wave packet well localized around the center position \mathbf{r}_c and the wave vector \mathbf{k}_c , constructed from the n th band as [55–57]

$$|W_n\rangle = \int d\mathbf{q} C_{k_c,n}(\mathbf{q}) e^{iq\cdot\hat{\mathbf{r}}} |u_{q,n}\rangle, \quad (11)$$

where $|W_n\rangle$ satisfies

$$\langle W_n | \hat{\mathbf{r}} | W_n \rangle = \mathbf{r}_c. \quad (12)$$

Here, the expansion coefficients $C_{k_c,n}(\mathbf{q})$ satisfy

$$\int d\mathbf{q} |C_{k_c,n}(\mathbf{q})|^2 = 1, \quad (13)$$

$$\int d\mathbf{q} |C_{k_c,n}(\mathbf{q})|^2 f(\mathbf{q}) \simeq f(\mathbf{k}_c), \quad (14)$$

for an arbitrary function $f(\mathbf{q})$. From Eqs. (1) and (8), the total one-body Hamiltonian is written as

$$\hat{H}_{\text{tot}} = \hat{H} + \sum_\lambda^{\text{Irrep.}} g_\lambda \hat{Q}_\lambda \varepsilon_\lambda(\hat{\mathbf{r}}). \quad (15)$$

We assume that the strain field varies slowly on the spatial scale of the wave packet. Thus, we can expand $\varepsilon_\lambda(\hat{\mathbf{r}})$ around \mathbf{r}_c :

$$\varepsilon_\lambda(\hat{\mathbf{r}}) = \varepsilon_\lambda(\mathbf{r}_c) + (\hat{\mathbf{r}} - \mathbf{r}_c) \cdot \nabla \varepsilon_\lambda + \dots \quad (16)$$

Hereafter, we omit the subscript c for notational simplicity. The equations of motion of the center position and the center wave vector read [57]

$$\dot{\mathbf{r}} = \frac{1}{\hbar} \frac{\partial \varepsilon_{k,n}(\mathbf{r})}{\partial \mathbf{k}}, \quad (17)$$

$$\hbar \dot{\mathbf{k}} = -\nabla \varepsilon_{k,n}(\mathbf{r}), \quad (18)$$

where $\varepsilon_{k,n}(\mathbf{r}) = \langle W_n | \hat{H}_{\text{tot}} | W_n \rangle$ and \hbar is the Dirac constant. Here, geometric contributions (e.g., Berry curvature terms) are omitted, as they are not relevant to the discussion below. Substituting Eq. (16) into Eq. (18), we obtain

$$\hbar \dot{\mathbf{k}} \simeq - \sum_{\lambda}^{\text{Irrep.}} g_{\lambda}(\hat{Q}_{\lambda,k})_n \nabla \epsilon_{\lambda}, \quad (19)$$

where $(\hat{Q}_{\lambda,k})_n = \langle W_n | \hat{Q}_{\lambda} | W_n \rangle \simeq \langle u_{k,n} | \hat{Q}_{\lambda} | u_{k,n} \rangle$. Equation (19) shows that a finite strain gradient acts as a driving force and thus accelerates the electron wavepacket, leading to a shift of the electronic distribution in momentum space (an asymmetric distribution).

In the presence of dissipation, the nonequilibrium steady state with the asymmetric distribution can be sustained. The term *flexocurrent* is defined as the shorthand for the current induced by $\nabla \epsilon_{\lambda}$. In systems with spin-momentum splittings in the electronic band structure [see Fig. 1(a) for Rashba systems], this nonequilibrium distribution is expected to result in a finite magnetization, as shown in Fig. 1(b). We refer to this nonequilibrium magnetization response as FCIM. FCIM is analogous to CIM and constitutes a dissipative part of nonequilibrium response in metals. Therefore, this effect can be formulated by evaluating the dissipative component of the adiabatic magnetization response tensor within the Kubo's linear response theory [51].

D. Magnetization response to strain gradient

In this section, we formulate the linear response theory when general strain fields $\epsilon(\mathbf{r})$ are applied to the system, where Hamiltonian is given by Eq. (3). We introduce the adiabatic magnetization response tensor $f_{\alpha\beta}^{\lambda}$, which relates the macroscopic magnetization \bar{M}_{α} to the strain gradient $\nabla_{\beta} \epsilon_{\lambda}$ as

$$\bar{M}_{\alpha} = f_{\alpha\beta}^{\lambda} \nabla_{\beta} \epsilon_{\lambda}. \quad (20)$$

Here, the repeated indices are assumed to be summed over and the macroscopic magnetization is defined as $\bar{M}_{\alpha} = \frac{1}{V} \int d\mathbf{r} \langle M_{\alpha}(\mathbf{r}) \rangle$, where $\langle \dots \rangle$ stands for the thermal average and

$$M_{\alpha}(\mathbf{r}) = \Psi^{\dagger}(\mathbf{r}) \hat{M}_{\alpha} \Psi(\mathbf{r}) \quad (21)$$

is the local magnetization density. The operator \hat{M}_{α} is a one-body magnetization operator, such as the spin or orbital magnetic moment. To evaluate $f_{\alpha\beta}^{\lambda}$, we employ Luttinger's method [50] originally introduced to calculate the thermal average of observables induced by the spatial gradient of a scalar potential within the framework of Kubo linear response theory. This formalism provides the transport limit of the response ($\mathbf{q} \rightarrow 0$ then $\omega \rightarrow 0$). This corresponds to focusing on the nonequilibrium response. We apply this approach to the case of the strain field. We note that, by contrast, taking the static limit ($\omega \rightarrow 0$ then $\mathbf{q} \rightarrow 0$) amounts to probing the equilibrium response and corresponds to the conventional flexomagnetic effect [31, 32]. Introducing the density operator ρ ,

\bar{M}_{α} can be expressed as

$$\bar{M}_{\alpha} = \frac{1}{V} \int d\mathbf{r} \text{Tr}[\rho M_{\alpha}(\mathbf{r})]. \quad (22)$$

Within linear response theory, ρ is given by

$$\rho = -\rho_{\text{eq}} \int dt e^{-\delta t} \int_0^{\frac{1}{k_B T}} ds \dot{\mathcal{V}}(-t - i\hbar s), \quad (23)$$

where ρ_{eq} is the equilibrium density operator in the absence of external fields, k_B is the Boltzmann constant, T is the temperature, and δ is a positive infinitesimal constant. Here, $\dot{\mathcal{V}}$ denotes the time derivative of the perturbation [Eq. (8)], and the time evolution of an operator is defined in the Heisenberg representation as $O(t) = e^{i\mathcal{H}t/\hbar} O e^{-i\mathcal{H}t/\hbar}$. To evaluate $\dot{\mathcal{V}}$, we calculate the time derivative of $Q_{\lambda}(\mathbf{r})$. The Heisenberg equation leads to

$$\begin{aligned} \dot{Q}_{\lambda}(\mathbf{r}) &= \frac{i}{\hbar} [\mathcal{H}, Q_{\lambda}(\mathbf{r})] \\ &= -\nabla \cdot \mathbf{J}^{\lambda}(\mathbf{r}) + \tau^{\lambda}(\mathbf{r}), \end{aligned} \quad (24)$$

where we have introduced the electric quadrupole current $\mathbf{J}^{\lambda}(\mathbf{r})$ and torque densities $\tau^{\lambda}(\mathbf{r})$ as

$$\mathbf{J}^{\lambda}(\mathbf{r}) = \frac{1}{2} [\Psi^{\dagger}(\mathbf{r}) \hat{\mathbf{J}}^{\lambda} \Psi(\mathbf{r}) + \text{H.c.}], \quad (25)$$

$$\tau^{\lambda}(\mathbf{r}) = \frac{1}{2} [\Psi^{\dagger}(\mathbf{r}) \hat{\tau}^{\lambda} \Psi(\mathbf{r}) + \text{H.c.}], \quad (26)$$

Here, using the velocity operator defined as $\hat{\mathbf{v}} = \frac{i}{\hbar} [\hat{H}, \hat{\mathbf{r}}]$, we can express their one-body operators as $\hat{\mathbf{J}}^{\lambda} = \frac{1}{2} (\hat{\mathbf{v}} \hat{Q}_{\lambda} + \hat{Q}_{\lambda} \hat{\mathbf{v}})$ and $\hat{\tau}^{\lambda} = \frac{i}{\hbar} [\hat{H}, \hat{Q}_{\lambda}]$. Note that Eqs. (25) and (26) remain valid even when \hat{Q}_{λ} is nonlocal. Using Eqs. (8), (24), (25), and (26), we obtain

$$\begin{aligned} \dot{\mathcal{V}} &= \sum_{\lambda}^{\text{Irrep.}} g_{\lambda} \int d\mathbf{r} \epsilon_{\lambda}(\mathbf{r}) \dot{Q}_{\lambda}(\mathbf{r}) \\ &= \sum_{\lambda}^{\text{Irrep.}} g_{\lambda} \int d\mathbf{r} [\mathbf{J}^{\lambda}(\mathbf{r}) \cdot \nabla \epsilon_{\lambda}(\mathbf{r}) + \tau^{\lambda}(\mathbf{r}) \epsilon_{\lambda}(\mathbf{r})], \end{aligned} \quad (27)$$

where we have carried out integration by parts for the first term. Hence, \bar{M}_{α} is given by

$$\begin{aligned} \bar{M}_{\alpha} &= -\frac{1}{V} \sum_{\lambda}^{\text{Irrep.}} g_{\lambda} \int dt e^{-\delta t} \int_0^{\frac{1}{k_B T}} ds \int d\mathbf{r} \int d\mathbf{r}' \\ &\quad \times \left\{ \sum_{\beta} \langle J_{\beta}^{\lambda}(\mathbf{r}, -i\hbar s) M_{\alpha}(\mathbf{r}', t) \rangle_{\text{eq}} \nabla_{\beta} \epsilon_{\lambda}(\mathbf{r}) \right. \\ &\quad \left. + \langle \tau^{\lambda}(\mathbf{r}, -i\hbar s) M_{\alpha}(\mathbf{r}', t) \rangle_{\text{eq}} \epsilon_{\lambda}(\mathbf{r}) \right\}, \end{aligned} \quad (28)$$

where $\langle \dots \rangle_{\text{eq}}$ denotes the thermal average in equilibrium before applying the external field $\epsilon(\mathbf{r})$ at $t = -\infty$. Thus, $f_{\alpha\beta}^{\lambda}$ can be expressed as

$$f_{\alpha\beta}^{\lambda} = f_{\alpha\beta}^{\lambda(1)} + f_{\alpha\beta}^{\lambda(2)}, \quad (29)$$

with

$$f_{\alpha\beta}^{\lambda(1)} = -\frac{g_\lambda}{V} \int dt e^{-\delta t} \int_0^{\frac{1}{k_B T}} ds \langle J_{\beta,-q=0}^\lambda(-i\hbar s) M_{\alpha,q=0}(t) \rangle_{\text{eq}}, \quad (30)$$

$$f_{\alpha\beta}^{\lambda(2)} = -\frac{g_\lambda}{V} \int dt e^{-\delta t} \int_0^{\frac{1}{k_B T}} ds \frac{\partial}{\partial i q_\beta} \left[\langle \tau_{-q}^\lambda(-i\hbar s) M_{\alpha,q}(t) \rangle_{\text{eq}} \right]_{q=0}. \quad (31)$$

Here, $J_{\beta,q}^\lambda = \int d\mathbf{r} e^{-iq\cdot\mathbf{r}} J_\beta^\lambda(\mathbf{r})$, $\tau_q^\lambda = \int d\mathbf{r} e^{-iq\cdot\mathbf{r}} \tau^\lambda(\mathbf{r})$, and $M_{\alpha,q} = \int d\mathbf{r} e^{-iq\cdot\mathbf{r}} M_\alpha(\mathbf{r})$. The derivation of $f_{\alpha\beta}^{\lambda(2)}$ in Eq. (31) is provided in Appendix A.

The response tensor $f_{\alpha\beta}^{\lambda}$ contains both dissipative and nondissipative contributions. To evaluate FCIM, we focus on the dissipative contributions. The dissipative parts of $f_{\alpha\beta}^{\lambda(1)}$ and $f_{\alpha\beta}^{\lambda(2)}$ are denoted by $f_{\alpha\beta}^{\lambda(1):\text{dis}}$ and $f_{\alpha\beta}^{\lambda(2):\text{dis}}$, respectively, and are given by

$$f_{\alpha\beta}^{\lambda(1):\text{dis}} = \frac{\hbar g_\lambda}{V\eta} \sum_k \sum_{n=1}^N (\hat{M}_{\alpha,k})_n (\hat{J}_{\beta,k}^\lambda)_n \frac{\partial f(\varepsilon_{k,n})}{\partial \varepsilon_{k,n}}, \quad (32)$$

$$f_{\alpha\beta}^{\lambda(2):\text{dis}} = -\frac{\hbar g_\lambda}{V\eta} \sum_k \sum_{n=1}^N \sum_{m(\neq n)}^N (\hat{M}_{\alpha,k})_n \text{Re}[(\hat{v}_{\beta,k})_{nm} (\hat{Q}_{\lambda,k})_{mn}] \times \frac{\partial f(\varepsilon_{k,n})}{\partial \varepsilon_{k,n}}, \quad (33)$$

where η is a phenomenological damping rate originating from nonmagnetic impurity scatterings, and $f(x) = [e^{\beta(x-\mu)} + 1]^{-1}$ denotes the Fermi distribution function with the chemical potential μ . A detailed derivation of Eqs. (32) and (33) is provided in Appendix B. We have introduced the Bloch representation of a one-body operator $\hat{\delta}_k = e^{-ik\cdot\mathbf{r}} \hat{\delta} e^{ik\cdot\mathbf{r}}$, and define its matrix elements on the band basis as $(\hat{\delta}_k)_n = (U_k^\dagger \hat{\delta}_k U_k)_{nn}$ and $(\hat{\delta}_k)_{nm} = (U_k^\dagger \hat{\delta}_k U_k)_{nm}$. Note that since \hat{Q}_λ does not contain the momentum operator, we have $e^{-ik\cdot\mathbf{r}} \hat{Q}_\lambda e^{ik\cdot\mathbf{r}} = \hat{Q}_\lambda$. Equation (32) represents the contribution induced by the electric quadrupole current, which can be regarded as the counterpart of CIM. In CIM, the electric quadrupole current in Eq. (32) is replaced by the electric current [58, 59]. Equation (33) corresponds to the contribution induced by the electric quadrupole torque. We note that in CIM, no analogous torque term [Eq. (33)] appears because the scalar potential couples with the charge density, which always satisfies the continuity equation. Using the relation $(\hat{J}_{\beta,k}^\lambda)_n = \text{Re} \sum_{m=1}^N (\hat{v}_{\beta,k})_{nm} (\hat{Q}_{\lambda,k})_{mn}$, the total response coefficient $f_{\alpha\beta}^{\lambda:\text{dis}}$ can be written as

$$\begin{aligned} f_{\alpha\beta}^{\lambda:\text{dis}} &= f_{\alpha\beta}^{\lambda(1):\text{dis}} + f_{\alpha\beta}^{\lambda(2):\text{dis}} \\ &= \frac{\hbar g_\lambda}{V\eta} \sum_k \sum_{n=1}^N (\hat{M}_{\alpha,k})_n (\hat{v}_{\beta,k})_n (\hat{Q}_{\lambda,k})_n \frac{\partial f(\varepsilon_{k,n})}{\partial \varepsilon_{k,n}}. \end{aligned} \quad (34)$$

When the torque is absent, i.e., $[\hat{H}_k, \hat{Q}_\lambda] = 0$, all the off-diagonal interband components $(\hat{Q}_{\lambda,k})_{mn}$ with $m \neq n$ vanish, and Eq. (32) reduces to Eq. (34).

We note that it is straightforward to check that Eq. (34) agrees exactly with the expression obtained from the semiclassical theory. One can follow the discussion in Ref. [60]. Using the semiclassical Boltzmann transport equation under Eqs. (17), (18), and (19), one finds that the Fermi surface contribution to the nonequilibrium magnetization coincides with Eq. (34).

E. Symmetry arguments under spatial inversion and time-reversal operations

In this section, we discuss how presence or absence of the spatial inversion and time-reversal symmetries gives conditions for a finite FCIM. In systems with spatial inversion symmetry, the one-body operators appearing in Eq. (34) satisfy $\mathcal{I} \hat{H}_k \mathcal{I}^{-1} = \hat{H}_{-k}$, $\mathcal{I} \hat{v}_k \mathcal{I}^{-1} = -\hat{v}_{-k}$, $\mathcal{I} \hat{Q}_\lambda \mathcal{I}^{-1} = \hat{Q}_\lambda$, and $\mathcal{I} \hat{M}_k \mathcal{I}^{-1} = \hat{M}_{-k}$, where \mathcal{I} denotes the spatial inversion operator. Thus, Eq. (34) with the dummy variable $\mathbf{k} \rightarrow -\mathbf{k}$ reads

$$\begin{aligned} f_{\alpha\beta}^{\lambda:\text{dis}} &= \frac{\hbar g_\lambda}{V\eta} \sum_k \sum_{n=1}^N \left[(+\hat{M}_{\alpha,k})_n (-\hat{v}_{\beta,k})_n (+\hat{Q}_{\lambda,k})_n \frac{\partial f(\varepsilon_{k,n})}{\partial \varepsilon_{k,n}} \right] \\ &= -f_{\alpha\beta}^{\lambda:\text{dis}}. \end{aligned} \quad (35)$$

Thus, FCIM vanishes in systems with spatial inversion symmetry. Whereas the spatial inversion symmetry forces FCIM to vanish, the TRS does not impose any constraint on FCIM. In systems with TRS, the operators transform as $\Theta \hat{H}_k \Theta^{-1} = \hat{H}_{-k}$, $\Theta \hat{v}_k \Theta^{-1} = -\hat{v}_{-k}$, $\Theta \hat{Q}_\lambda \Theta^{-1} = \hat{Q}_\lambda$, and $\Theta \hat{M}_k \Theta^{-1} = -\hat{M}_{-k}$, where Θ denotes the time-reversal operator. Noting that there are two time-reversal odd operators in Eq. (34), one obtains no condition due to time-reversal invariance. Therefore, breaking the spatial inversion symmetry is sufficient to obtain a finite response; breaking the TRS is not required for this effect.

The same conclusion is reached more directly from symmetry considerations of the correlation function [Eq. (28)]. From Eq. (30), $f_{\alpha\beta}^{\lambda(1):\text{dis}}$ transforms as $M_\alpha J_\beta^\lambda$, where J_β^λ is odd under both spatial inversion and time-reversal operations, while M_α is even under spatial inversion and odd under time-reversal operations. Therefore, $f_{\alpha\beta}^{\lambda(1):\text{dis}}$ can be finite in systems that break the spatial inversion symmetry, regardless of whether the TRS is preserved. Similarly, from Eq. (31) [or Eq. (B3)], $f_{\alpha\beta}^{\lambda(2):\text{dis}}$ transforms as $M_\alpha v_\beta \tau^\lambda$, leading to the same conclusion. There exist 21 crystallographic point groups without spatial inversion symmetry. Group-theoretical analysis indicates that the FCIM response is allowed in all of them. Moreover, for each

TABLE I. Symmetry properties under spatial inversion \mathcal{P} and time-reversal \mathcal{T} .

Quantities	Symbol	\mathcal{P}	\mathcal{T}
Strain gradient	$\nabla \varepsilon_\lambda$	-	+
Electric quadrupole current	\mathbf{J}^λ	-	-
Electric quadrupole torque	τ^λ	+	-
Magnetization	\mathbf{M}	+	-

of these 21 point groups, all components of the magnetization can, in principle, be finite. That is, for each $\alpha \in (x, y, z)$, there exist at least one index pair (β, λ) with nonzero $f_{\alpha\beta}^{\lambda:\text{dis}}$. We note that these arguments apply only to dissipative contributions, for which irreversible relaxation processes effectively break the TRS and relax the constraints on $f_{\alpha\beta}^{\lambda}$ owing to the opposite time-reversal parities of $\nabla_{\beta}\epsilon_{\lambda}$ and M_{α} . For the nondissipative contribution, there is no source that breaks the TRS, and the symmetry constraint must be analyzed in terms of $M_{\alpha}\nabla_{\beta}\epsilon_{\lambda}$. For this contribution, both spatial inversion and TRS must be broken to produce a finite magnetization response. Table I summarizes the symmetry properties of $\nabla\epsilon$, J^{λ} , τ^{λ} , and \mathbf{M} under the spatial inversion and time-reversal operations.

It should be emphasized that FCIM is distinct from the dynamical multiferroic effect [61, 62]. The dynamical multiferroic effect refers to the generation of a magnetization driven by a time-dependent electric polarization, defined as $\mathbf{M} \propto \mathbf{P} \times \dot{\mathbf{P}}$. The electric polarization responsible for this effect can arise from various microscopic origins, such as static displacements in ferroelectric materials and dynamical ionic motions associated with optical phonons. In contrast, the FCIM discussed in this paper does not require the polarization. The magnetization observed in nonmagnetic semiconductor silicon under strain gradients is attributed to the dynamical multiferroic effect [63].

III. APPLICATION TO NONMAGNETIC SYSTEMS

In this section, we apply our theory for FCIM to time-reversal symmetric systems without spatial inversion symmetry. As representative examples, we examine three noncentrosymmetric systems described by tight-binding models and evaluate their magnetization responses to strain gradients. The first model is based on a decorated square lattice obtained by slightly displacing the bond-centered sites of the Lieb lattice along the out-of-plane direction. The second example is a monolayer transition-metal dichalcogenide (TMDC), MoS₂, for which we employ the model constructed in Ref. [64]. The third model is a monolayer Janus MoSSe, which has the same structural polymorph as the second example, MoS₂. In the present study, we consider both macroscopic spin and orbital magnetizations, denoted by $\bar{\mathbf{S}}_{\alpha}$ and $\bar{\mathbf{L}}_{\alpha}$, respectively, and evaluate the corresponding response coefficients $f_{\alpha x}^{\lambda:\text{dis}}$. The definition of the x axis for each model is shown in Figs. 2(a) and 4(a). Throughout Sec. III, we set $\hbar = 1$ and define electric quadrupole operators to satisfy $\text{Tr}[\hat{Q}_{\lambda}\hat{Q}_{\lambda'}] = 2\delta_{\lambda,\lambda'}$.

A. Decorated square lattice

First, let us discuss the decorated square system. We consider a lattice structure composed of three sublattices; $l = 0$ (black) on the xy plane, while $l = 1$ (red) and 2 (red) slightly above the xy plane at the center of each bond between the $l = 0$ sites, as illustrated in Fig. 2(a), which is called the buckled Lieb lattice [65]. In the present study, we set the length of the primitive translation vectors to unity and assume that the

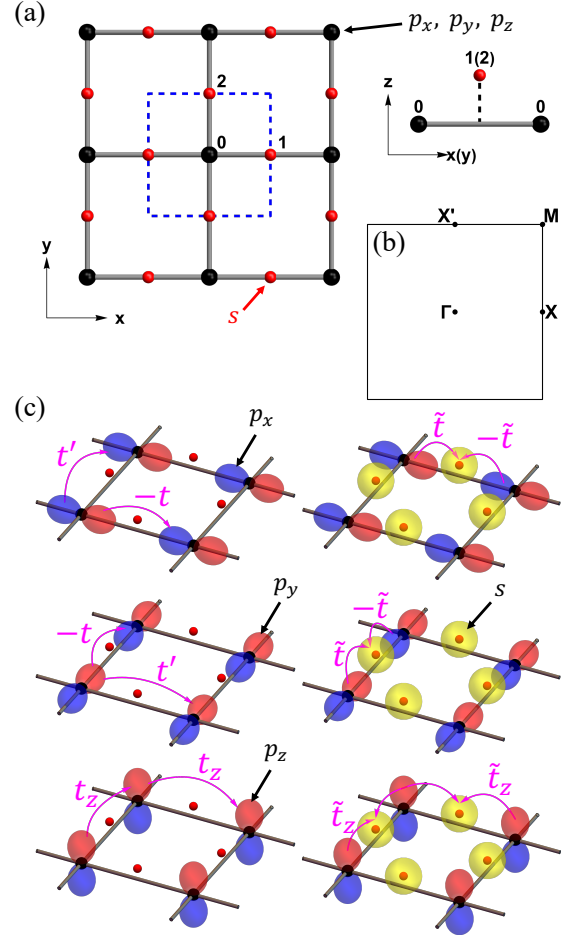


FIG. 2. (a) Schematic picture of the decorated square lattice. Black and red circles represent sites hosting p - and s -orbital degrees of freedom, respectively. The red sites are slightly elevated along the z direction. The blue dashed square indicates the unit cell. The numbers represent the sublattice indices. (b) Two-dimensional first Brillouin zone of the decorated square lattice. (c) Nearest-neighbor hoppings for p - p and p - s orbitals allowed in the present C_{4v} system.

sublattices $l = 0$ host p -orbital, while those for $l = 1$ and 2 do s -orbitals. Since the sites for the $l = 1$ and 2 sublattices are slightly elevated along the z direction, the system belongs to the C_{4v} point group, where a macroscopic electric polarization along the z direction is allowed. The creation and annihilation operators for the p -orbital on the sublattice $l = 0$ in the i th unit cell are denoted as $p_{i,\gamma\sigma}^{\dagger}$ and $p_{i,\gamma\sigma}$, where $\sigma = \uparrow, \downarrow$ and $\gamma = x, y, z$ represent the spin and the orbital indices, respectively. The corresponding operators for the s -orbitals on the sublattices $l = 1$ and 2 are represented as $s_{i,l\sigma}^{\dagger}$ and $s_{i,l\sigma}$, respectively. Thus, the Hamiltonian \mathcal{H} is written as

$$\mathcal{H} = \mathcal{H}_0 + \mathcal{H}_{\text{SO}} + \mathcal{H}_s, \quad (36)$$

$$\mathcal{H}_0 = \sum_{i,\sigma} \sum_{\gamma=x,y,z} \epsilon_{\gamma} p_{i,\gamma\sigma}^{\dagger} p_{i,\gamma\sigma} + \sum_{i,\sigma} \sum_{l=1,2} \epsilon_s s_{i,l\sigma}^{\dagger} s_{i,l\sigma}, \quad (37)$$

$$\mathcal{H}_{\text{SO}} = \lambda_{\text{SO}} \sum_{i,\sigma\sigma'} \sum_{\gamma\gamma'=x,y,z} p_{i,\gamma\sigma}^{\dagger} (\hat{\mathbf{L}} \cdot \hat{\mathbf{S}})_{\gamma\sigma,\gamma'\sigma'} p_{i,\gamma'\sigma'}, \quad (38)$$

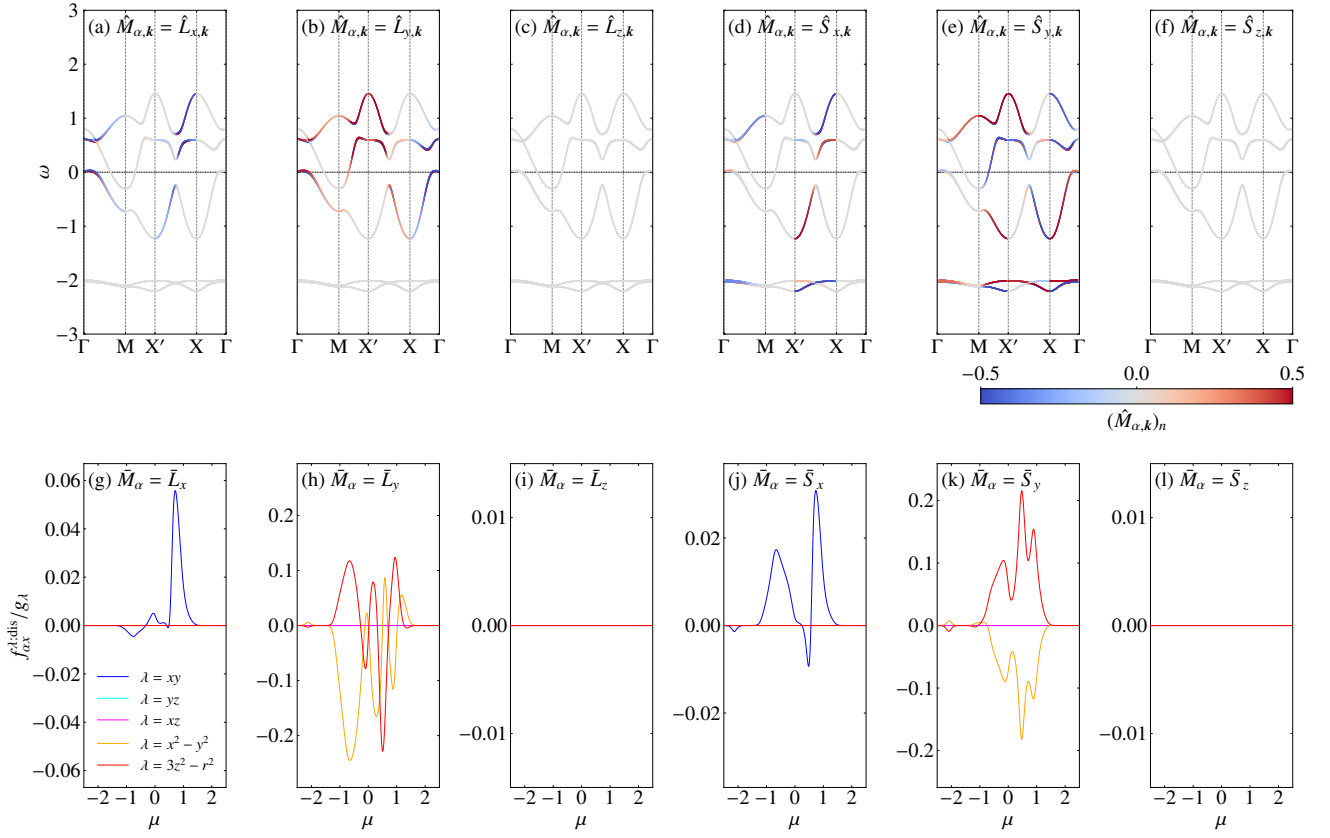


FIG. 3. [(a)–(f)] Band dispersions and color maps of (a) $(\hat{L}_{x,k})_n$, (b) $(\hat{L}_{y,k})_n$, (c) $(\hat{L}_{z,k})_n$, (d) $(\hat{S}_{x,k})_n$, (e) $(\hat{S}_{y,k})_n$, and (f) $(\hat{S}_{z,k})_n$ at $\varepsilon_s = -2$, $\varepsilon_{p_x} = \varepsilon_{p_y} = 0$, $\varepsilon_{p_z} = 0.6$, $t = 0.5$, $t' = 0.2$, $t_z = 0.1$, $\tilde{t}_z = 0.1$, $\tilde{t} = 0.2$, and $\lambda_{SO} = 0.4$. [(g)–(l)] Chemical potential dependence of $f_{\alpha x}^{\lambda:\text{dis}}/g_A$ for (g) \bar{L}_x , (h) \bar{L}_y , (i) \bar{L}_z , (j) \bar{S}_x , (k) \bar{S}_y , and (l) \bar{S}_z , with $k_B T = 0.05$ and $\eta = 0.05$.

$$\begin{aligned}
\mathcal{H}_t = & \sum_{i,\sigma} \left\{ t(p_{i,x\sigma}^\dagger p_{i+\hat{a}_1,x\sigma} + p_{i,y\sigma}^\dagger p_{i+\hat{a}_2,y\sigma} + \text{H.c.}) \right. \\
& - t'(p_{i,x\sigma}^\dagger p_{i+\hat{a}_2,x\sigma} + p_{i,y\sigma}^\dagger p_{i+\hat{a}_1,y\sigma} + \text{H.c.}) \\
& - t_z(p_{i,z\sigma}^\dagger p_{i+\hat{a}_1,z\sigma} + p_{i,z\sigma}^\dagger p_{i+\hat{a}_2,z\sigma} + \text{H.c.}) \\
& - \tilde{t}_z [p_{i,z\sigma}^\dagger (s_{i,1\sigma} + s_{i,2\sigma} + s_{i-\hat{a}_1,1\sigma} + s_{i-\hat{a}_2,2\sigma}) + \text{H.c.}] \\
& \left. - \tilde{t} [p_{i,x\sigma}^\dagger (s_{i,1\sigma} - s_{i-\hat{a}_1,1\sigma}) + p_{i,y\sigma}^\dagger (s_{i,2\sigma} - s_{i-\hat{a}_2,2\sigma}) + \text{H.c.}] \right\}. \quad (39)
\end{aligned}$$

Here, i labels the unit cell and the i th unit cell has four nearest-neighbor sites $i \pm \hat{a}_{1(2)}$ along the $\pm x$ ($\pm y$) direction. $\varepsilon_x = \varepsilon_y$, ε_z , and ε_s are the local energy levels for the $p_{x,y}$, p_z , and s -electrons, respectively. The hopping parameters t and the spin-orbit coupling (SOC) λ_{SO} are supposed to be positive. Equation (39) includes all nearest-neighbor hoppings between the orbitals p - p and p - s that are allowed by the C_{4v} symmetry. Each hopping process in Eq. (39) is illustrated in Fig. 2(b). For numerical calculations, the parameters are fixed as $\varepsilon_s = -2$, $\varepsilon_{p_x} = \varepsilon_{p_y} = 0$, $\varepsilon_{p_z} = 0.6$, $t = 0.5$, $t' = 0.2$, $t_z = 0.1$, $\tilde{t}_z = 0.1$, $\tilde{t} = 0.2$, and $\lambda_{SO} = 0.4$ as representative ones.

Within the p -orbital sector, local electric quadrupole moments are active, leading to a coupling with the strain [see Eq. (8)]. We introduce the electric quadrupole operators $Q_{i,\lambda}$

for the p -electron at the i th unit cell, which are written by

$$Q_{i,x^2-y^2} = \sum_{\sigma} (p_{i,x\sigma}^\dagger p_{i,x\sigma} - p_{i,y\sigma}^\dagger p_{i,y\sigma}), \quad (40)$$

$$Q_{i,3z^2-r^2} = \sum_{\sigma} \frac{1}{\sqrt{3}} (2p_{i,z\sigma}^\dagger p_{i,z\sigma} - p_{i,x\sigma}^\dagger p_{i,x\sigma} - p_{i,y\sigma}^\dagger p_{i,y\sigma}), \quad (41)$$

$$Q_{i,xy} = \sum_{\sigma} (p_{i,x\sigma}^\dagger p_{i,y\sigma} + \text{H.c.}), \quad (42)$$

$$Q_{i,yz} = \sum_{\sigma} (p_{i,y\sigma}^\dagger p_{i,z\sigma} + \text{H.c.}), \quad (43)$$

$$Q_{i,xz} = \sum_{\sigma} (p_{i,z\sigma}^\dagger p_{i,x\sigma} + \text{H.c.}). \quad (44)$$

$Q_{i,\lambda}$ corresponds to $Q_{\lambda}(\mathbf{r})$ in the continuum systems. In the absence of strain, the system preserves the TRS, while lacking inversion symmetry. Therefore, $f_{\alpha\beta}^{\lambda:\text{dis}}$ can take a finite value.

Before presenting the numerical result for $f_{\alpha x}^{\lambda:\text{dis}}$, we first estimate in advance the components of $f_{\alpha x}^{\lambda:\text{dis}}$ that are allowed by symmetry under the C_{4v} point group. As discussed in Sec. II E, TRS is irrelevant to the response of $f_{\alpha\beta}^{\lambda:\text{dis}}$, and therefore it does not need to be considered. From the definition in Eq. (20), the scalar quantity constructed from $f_{\alpha\beta}^{\lambda:\text{dis}}$ and $\bar{M}_{\alpha} \nabla_{\beta} \epsilon_{\lambda}$ necessarily belongs to the trivial representation i.e., A_1 representation which is invariant in the C_{4v} group. Accord-

ing to Neumann's principles, in the absence of any symmetry-breaking order parameters, $f_{\alpha\beta}^{A:\text{dis}}$ belongs to the trivial representation. Thus, $\bar{M}_\alpha \nabla_\beta \epsilon_{\lambda}$ must also belong to the trivial representation. From Table II, the combinations of $\bar{M}_\alpha \nabla_\beta \epsilon_{\lambda}$ that transform according to the A_1 representation are

$$\begin{aligned} & \bar{M}_y \nabla_y \epsilon_{xy} - \bar{M}_x \nabla_x \epsilon_{xy}, \\ & \bar{M}_y \nabla_x \epsilon_{x^2-y^2} + \bar{M}_x \nabla_y \epsilon_{x^2-y^2}, \\ & \bar{M}_y \nabla_x \epsilon_{3z^2-r^2} - \bar{M}_x \nabla_y \epsilon_{3z^2-r^2}, \\ & \bar{M}_z (\nabla_x \epsilon_{yz} - \nabla_y \epsilon_{xz}). \end{aligned}$$

Thus, in the C_{4v} point group, the nonzero components of $f_{\alpha x}^{A:\text{dis}}$ are $f_{xx}^{xy:\text{dis}}$, $f_{yx}^{x^2-y^2:\text{dis}}$, $f_{yx}^{3z^2-r^2:\text{dis}}$, and $f_{zx}^{yz:\text{dis}}$. This conclusion can also be verified by explicitly applying the symmetry operations of the C_{4v} point group to $f_{\alpha\beta}^{A:\text{dis}}$.

Figures 3(a)–3(f) show the electronic band dispersions along with color maps of the expectation values of the angular momenta $(\hat{M}_{\alpha,k})_n = (\hat{L}_{\alpha,k})_n, (\hat{S}_{\alpha,k})_n$ ($\alpha = x, y, z$) for each band. These plots clearly indicate finite expectation values of $\hat{L}_{x,k}$, $\hat{L}_{y,k}$, $\hat{S}_{x,k}$, and $\hat{S}_{y,k}$, as shown in Figs. 3(a), 3(b), 3(d), and 3(e). This behavior can be understood from the symmetry properties of the C_{4v} point group, which allow Rashba-type momentum dependent couplings. Both (k_x, k_y) and $(\hat{M}_y, -\hat{M}_x)$ form the basis of the E representation, and thus momentum-dependent terms of the form $k_x \hat{M}_y - k_y \hat{M}_x$ are symmetry-allowed. Accordingly, the momentum-space Hamiltonian can contain terms such as $\alpha_L (k_x \hat{L}_y - k_y \hat{L}_x) + \alpha_S (k_x \hat{S}_y - k_y \hat{S}_x)$, where α_L and α_S denote coupling constants. The orbital contribution arises from indirect hopping processes in which the p_x - and p_y -orbitals hybridize with the p_z -orbital through the s -orbitals at the bond center. This mechanism does not rely on the SOC and appears when both \tilde{t}_z and \tilde{t} are finite. An effective p -orbital Hamiltonian obtained by the Schrieffer-Wolff transformation yields $\alpha_L \sim \tilde{t}_z \tilde{t}$. The second term corresponds to the Rashba spin-orbit interaction with $\alpha_S \sim \lambda_{\text{SO}} \alpha_L$. Therefore, in systems with nonzero \tilde{t}_z , \tilde{t} , and λ_{SO} , finite expectation values of $\hat{L}_{x,k}$, $\hat{L}_{y,k}$, $\hat{S}_{x,k}$, and $\hat{S}_{y,k}$ are naturally expected. In contrast, the expectation values of $\hat{L}_{z,k}$ and $\hat{S}_{z,k}$ vanish for all bands and momenta, as shown in Figs. 3(c) and 3(f). Since \hat{M}_z belongs to the A_2 representation, the orbital terms such as $k_x k_y (k_x^2 - k_y^2) \hat{L}_z$ are symmetry-allowed in principle. However,

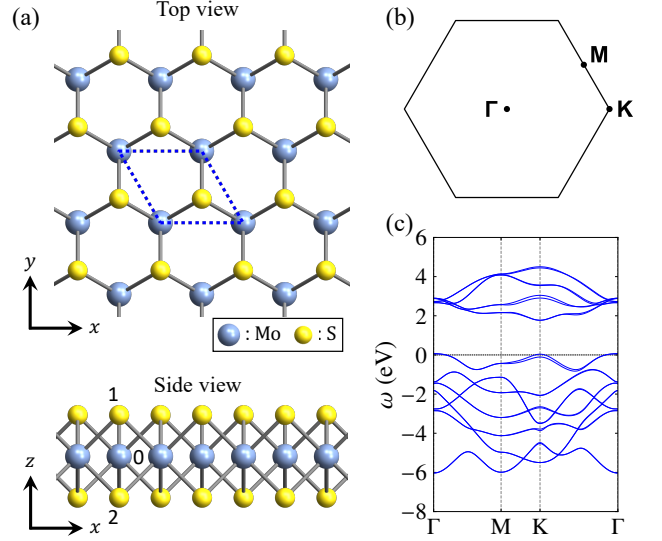


FIG. 4. (a) Top and side views of monolayer MoS₂. The blue dashed rhombus denotes the unit cell. The numbers in the side view represent the sublattice indices. (b) First Brillouin zone of monolayer MoS₂. (c) Band structure of monolayer MoS₂ calculated using the tight-binding model in Ref. [64].

in the absence of hopping between p_x - and p_y -orbitals, such terms do not appear, and hence $(\hat{L}_{z,k})_n$ are zero everywhere in the momentum space. The same argument applies to \hat{S}_z .

Figures 3(g)–3(l) show the chemical potential dependence of $f_{\alpha x}^{A:\text{dis}}/g_\lambda$ for \bar{L}_α and \bar{S}_α . See Eq. (22). As shown in Figs. 3(g), 3(h), 3(j), and 3(k), the responses of \bar{L}_x , \bar{L}_y , \bar{S}_x , and \bar{S}_y are finite. This behavior can be understood from the fact that $(\hat{L}_{x,k})_n$, $(\hat{L}_{y,k})_n$, $(\hat{S}_{x,k})_n$, and $(\hat{S}_{y,k})_n$ are finite [see Figs. 3(a), 3(b), 3(d), and 3(e)]. Furthermore, \bar{L}_x and \bar{S}_x are induced by $\nabla_x \epsilon_{xy}$, whereas \bar{L}_y and \bar{S}_y are induced by $\nabla_x \epsilon_{x^2-y^2}$ and $\nabla_x \epsilon_{3z^2-r^2}$, in complete agreement with the symmetry arguments. In contrast, as shown in Figs. 3(i) and 3(l), the responses of \bar{L}_z and \bar{S}_z are zero for all chemical potentials. This is consistent with the fact that $(\hat{L}_{z,k})_n$ and $(\hat{S}_{z,k})_n$ are zero for all bands and momenta [see Figs. 3(c) and 3(f)].

B. Monolayer MoS₂

Next, we evaluate the magnetization response to strain gradients using a tight-binding model for a monolayer MoS₂. The monolayer MoS₂ exhibits several structural polymorphs, such as $1H$, $1T$, and $1T'$ [66, 67]. In this study, we focus on the $1H$ structure with the D_{3h} point group as illustrated in Fig. 4(a). This structure consists of ABA stacking, where the top and bottom chalcogen atoms, labeled as sublattices 1 and 2, are projected onto the same in-plane position in the top view. The $1H$ -MoS₂ is a nonmagnetic direct-gap semiconductor with the band gap located at the K and K' points in the Brillouin zone. Following Ref. [64], we set the length of the primitive translation vectors to 3.18 Å and construct the tight-binding model including d -orbitals on the Mo sites and the p -orbitals on the S

TABLE II. Classification of $\nabla \epsilon_\lambda$ and \bar{M} according to the irreducible representations of the C_{4v} point group.

Basis	Irrep.
$\nabla_x \epsilon_{xz} + \nabla_y \epsilon_{yz}$	A_1
$\nabla_x \epsilon_{yz} - \nabla_y \epsilon_{xz}$	A_2
$\nabla_x \epsilon_{xz} - \nabla_y \epsilon_{yz}$	B_1
$\nabla_x \epsilon_{yz} + \nabla_y \epsilon_{xz}$	B_2
$(\nabla_y \epsilon_{xy}, \nabla_x \epsilon_{xy})$	E
$(\nabla_x \epsilon_{x^2-y^2}, -\nabla_y \epsilon_{x^2-y^2})$	E
$(\nabla_x \epsilon_{3z^2-r^2}, \nabla_y \epsilon_{3z^2-r^2})$	E
\bar{M}_z	A_2
$(\bar{M}_y, -\bar{M}_x)$	E

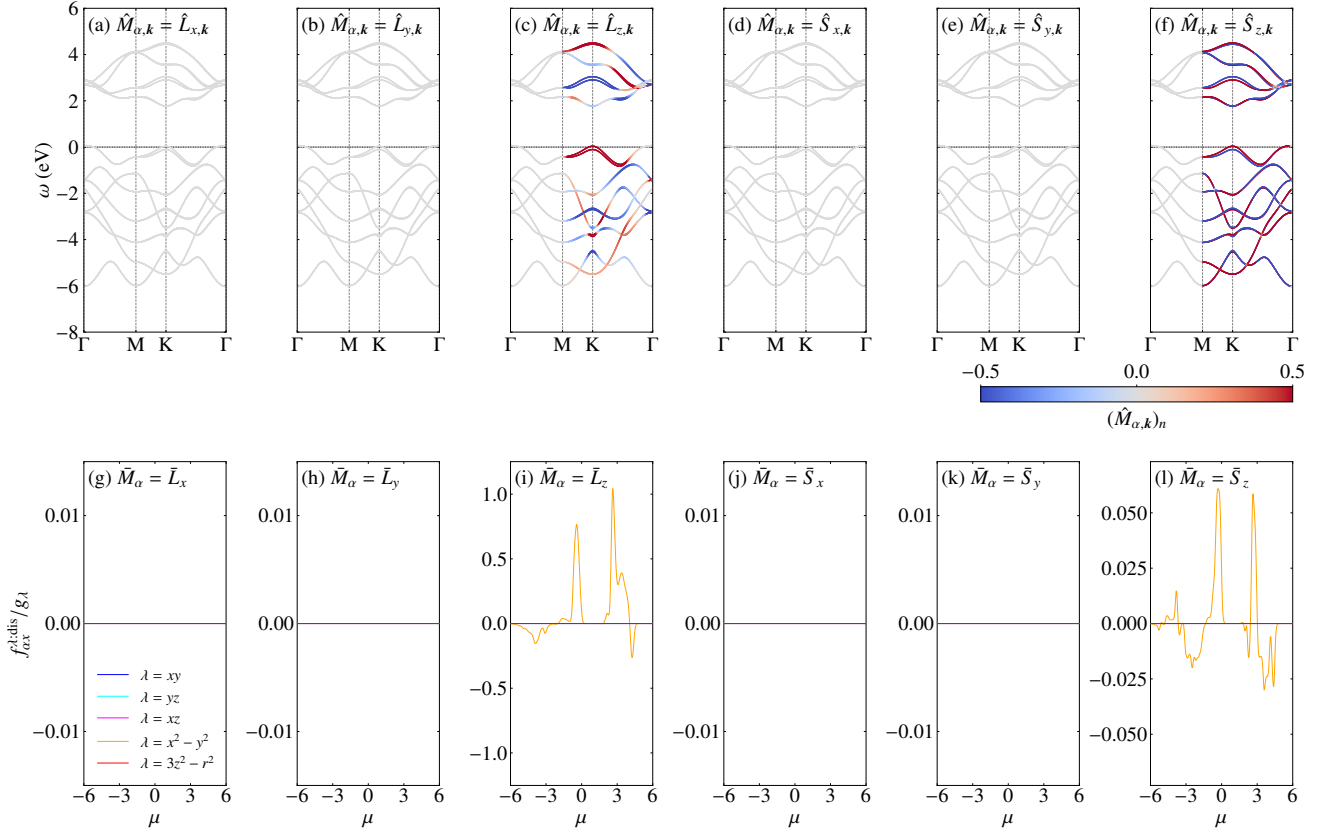


FIG. 5. [(a)–(f)] Band dispersions and color maps of (a) $(\hat{L}_{x,k})_n$, (b) $(\hat{L}_{y,k})_n$, (c) $(\hat{L}_{z,k})_n$, (d) $(\hat{S}_{x,k})_n$, (e) $(\hat{S}_{y,k})_n$, and (f) $(\hat{S}_{z,k})_n$ for monolayer MoS₂. [(g)–(l)] Chemical potential dependence of $f_{\alpha x}^{l:\text{dis}}/g_l$ for (g) \bar{L}_x , (h) \bar{L}_y , (i) \bar{L}_z , (j) \bar{S}_x , (k) \bar{S}_y , and (l) \bar{S}_z , with $k_B T = 0.05$ and $\eta = 0.05$. The length of primitive translation vectors is set to 3.18 Å in (g)–(l) [64].

sites. This setup effectively captures all orbitals relevant to the Fermi level in monolayer MoS₂. We have confirmed that the calculated band structure and the magnitude of spin splitting are consistent with Ref. [64]. The band dispersion of MoS₂ with SOC is shown in Fig. 4(c). The electric quadrupole degrees of freedom are active in both the p - and d -orbitals and are coupled with an external strain field. For simplicity, we

TABLE III. Classification of $\nabla\epsilon_l$ and \bar{M} according to the irreducible representations of the D_{3h} point group. Note that the inner product in $E' \otimes E''$ gives the A_2'' representation in the present arrangement in this table.

Basis	Irrep.
$2\nabla_x\epsilon_{xy} + \nabla_y\epsilon_{x^2-y^2}$	A_1'
$\nabla_x\epsilon_{x^2-y^2} - 2\nabla_y\epsilon_{xy}$	A_2'
$(\nabla_x\epsilon_{x^2-y^2} + 2\nabla_y\epsilon_{xy}, 2\nabla_x\epsilon_{xy} - \nabla_y\epsilon_{x^2-y^2})$	E'
$(\nabla_x\epsilon_{3z^2-r^2}, \nabla_y\epsilon_{3z^2-r^2})$	E'
$\nabla_x\epsilon_{yz} - \nabla_y\epsilon_{xz}$	A_1''
$\nabla_x\epsilon_{xz} + \nabla_y\epsilon_{yz}$	A_2''
$(\nabla_x\epsilon_{yz} + \nabla_y\epsilon_{xz}, \nabla_x\epsilon_{xz} - \nabla_y\epsilon_{yz})$	E''
\bar{M}_z	A_2'
$(\bar{M}_y, -\bar{M}_x)$	E''

consider only the electric quadrupoles constructed from the d -orbitals at the Mo sites, since the local nature of the d electrons is more important in the discussion of the strain effects than that of the p electrons at the S sites. The explicit forms of the electric quadrupole moments are given in Appendix C. Since the D_{3h} point group lacks spatial inversion symmetry, nonzero values of $f_{\alpha x}^{l:\text{dis}}$ are expected. We note that CIM is symmetry-forbidden in D_{3h} point group.

Before presenting the numerical results, we determine, on symmetry grounds, which components of $f_{\alpha x}^{l:\text{dis}}$ are finite in the D_{3h} point group. As discussed in Sec. III A, if TRS is not included as a symmetry operation, the scalar quantity composed of $f_{\alpha\beta}^{l:\text{dis}}\bar{M}_\alpha\nabla_\beta\epsilon_\lambda$ belongs to the trivial representation. Since monolayer MoS₂ does not exhibit any spontaneous order, $f_{\alpha\beta}^{l:\text{dis}}$ belongs to the trivial representation. Consequently, the combination of $\bar{M}_\alpha\nabla_\beta\epsilon_\lambda$ must also form a basis of the trivial representation. From Table III, the combinations of $\bar{M}_\alpha\nabla_\beta\epsilon_\lambda$ that form the basis of the A_1' representation are

$$\begin{aligned} &\bar{M}_y(\nabla_x\epsilon_{yz} + \nabla_y\epsilon_{xz}) - \bar{M}_x(\nabla_x\epsilon_{xz} - \nabla_y\epsilon_{yz}), \\ &\bar{M}_z(\nabla_x\epsilon_{x^2-y^2} - 2\nabla_y\epsilon_{xy}). \end{aligned} \quad (45)$$

Therefore, $f_{xx}^{xz:\text{dis}} = -f_{yx}^{yz:\text{dis}}$ and $f_{zx}^{x^2-y^2:\text{dis}}$ are finite, while the others vanish.

Figures 5(a)–5(f) show the color maps of $(\hat{M}_{\alpha,k})_n$ for each

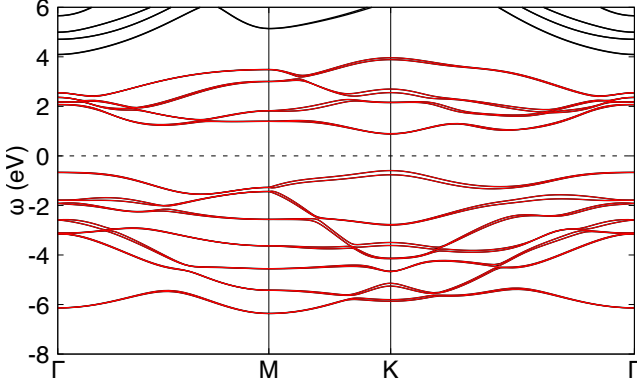


FIG. 6. Band structure of monolayer Janus MoSSe obtained from DFT calculation. The red curves indicate the bands for the effective tight-binding model.

band. In Figs. 5(a), 5(b), 5(d) and 5(e), one finds that $(\hat{L}_{x,k})_n$, $(\hat{L}_{y,k})_n$, $(\hat{S}_{x,k})_n$, and $(\hat{S}_{y,k})_n$ are zero for all bands and momenta. This behavior can be understood from the symmetry-allowed couplings between the wave vector and the magnetization under the D_{3h} point group. The lowest-order coupling term involving $\hat{M}_x(\hat{M}_y)$ takes the following form: $k_z[2k_x k_y \hat{M}_y - (k_x^2 - k_y^2)\hat{M}_x]$. Since there is no k_z component in two-dimensional systems, the expectation values of \hat{L}_x , \hat{L}_y , \hat{S}_x , and \hat{S}_y are zero. In contrast, Figs. 5(c) and 5(f) show that $(\hat{L}_{z,k})_n$ and $(\hat{S}_{z,k})_n$ are nonzero. This can be understood from the fact that \mathbf{k} and \hat{M}_z can couple under the D_{3h} symmetry in the following form: $k_x(k_x^2 - 3k_y^2)\hat{M}_z$. It is also confirmed that both $(\hat{L}_{z,k})_n$ and $(\hat{S}_{z,k})_n$ vanish along the Γ -M path, which is consistent with the relation $k_x^2 - 3k_y^2 = 0$ along this line and with the results of Ref. [68]. Figures 5(g)–5(l) show the chemical potential dependence of $f_{\alpha\lambda}^{l:\text{dis}}/g_\lambda$ for \bar{L}_α and \bar{S}_α . From Figs. 5(g), 5(h), 5(j), and 5(k), we find that the responses of $\bar{M}_\alpha = \bar{L}_x$, \bar{L}_y , \bar{S}_x , and \bar{S}_y vanish, which can be easily understood from the fact that $(\hat{M}_{\alpha,k})_n$ is identically zero for all bands and momenta. For $\bar{M}_\alpha = \bar{L}_z$ and \bar{S}_z , the responses induced by $\nabla_x \epsilon_{x^2-y^2}$ are finite, as shown in Figs. 5(h) and 5(l), in full agreement with the symmetry arguments. In addition, the magnitude of $f_{\alpha\lambda}^{l:\text{dis}}/g_\lambda$ is strongly enhanced near $\mu \sim 0$. This enhancement originates from the large value of $(\hat{M}_{z,k})_n$ around the M and K points near the valence band edge [see Figs. 5(c) and 5(d)]. Therefore, it is possible to observe a finite FCIM for $\nabla_x \epsilon_{xx}$ or $\nabla_x \epsilon_{yy}$ via hole doping in monolayer MoS₂ or metallic TMDCs such as NbS₂ [69, 70].

C. Monolayer MoSSe

Finally, we present the FCIM results for a monolayer Janus MoSSe [71, 72]. The monolayer Janus MoSSe is a member of the TMDC family and can be obtained from MoS₂ by substituting the S atoms on the top or bottom chalcogen layer with Se [73]. In this paper, we focus on the 1H-MoSSe structure obtained by replacing the top-layer S with Se in the monolayer MoS₂ shown in Fig. 4. The 1H-MoSSe is, similarly to

1H-MoS₂, a nonmagnetic semiconductor with a direct band gap at the K and K' points. In contrast, the substitution of the top-layer S by Se breaks the mirror symmetry with respect to the horizontal plane, lowering the point group from D_{3h} to C_{3v} . To determine the band structure of MoSSe, we perform density functional theory (DFT) calculations using Quantum ESPRESSO [74]. We first relax the crystal structure while keeping the interlayer Mo-Mo distance at 20 Å, and obtain an in-plane lattice constant of 3.251 Å for the length of the primitive translation vector. The resulting band structure is shown in Fig. 6. Focusing on the K point, we find a band gap of 1.48 eV, and estimate that the spin splittings of the uppermost valence and the lowermost conduction band are 0.17 eV and 0.013 eV, respectively, in good agreement with the previous study [75]. As in Sec. III B, to describe the bands near the Fermi level we construct an effective tight-binding model in a basis consisting of the d -orbitals on the Mo sites and the p -orbitals on the S and Se sites using Wannier90 [76, 77]. The resulting effective Hamiltonian is found to accurately reproduce the DFT bands highlighted by the red curves in Fig. 6. Although electric quadrupole degrees of freedom are active in the d -orbitals on the Mo sites and the p -orbitals on the S and Se sites, we consider only the electric quadrupole degrees of freedom originating from the d -orbitals, as in monolayer MoS₂ (Sec. III B), and calculate $f_{\alpha\lambda}^{l:\text{dis}}$.

Before showing the numerical results, we determine in advance the components of $f_{\alpha\lambda}^{l:\text{dis}}$ that can be nonzero under the C_{3v} symmetry. Since C_{3v} is a subgroup of D_{3h} , all responses allowed under D_{3h} are also allowed under C_{3v} . The important difference is that a finite electric dipole moment is allowed along the z direction in the C_{3v} point group symmetry. Consequently, the responses $f_{\alpha\beta}^{l:\text{dis}}$ that belong to the A_2' representation under D_{3h} are also allowed. This can be understood from the fact that an electric dipole along the z direction belongs to the A_2' representation in D_{3h} . Thus, from Table III, such A_2' components in $\bar{M}_\alpha \nabla_\beta \epsilon_\lambda$ are

$$\begin{aligned} \bar{M}_y(\nabla_x \epsilon_{x^2-y^2} + 2\nabla_y \epsilon_{xy}) - \bar{M}_x(2\nabla_x \epsilon_{xy} - \nabla_y \epsilon_{x^2-y^2}), \\ \bar{M}_y \nabla_x \epsilon_{3z^2-r^2} - \bar{M}_x \nabla_y \epsilon_{3z^2-r^2}, \\ \bar{M}_z(\nabla_x \epsilon_{yz} - \nabla_y \epsilon_{xz}). \end{aligned} \quad (46)$$

As a result, under the C_{3v} symmetry, the nonvanishing components of $f_{\alpha\lambda}^{l:\text{dis}}$ include, in addition to those already allowed under the D_{3h} symmetry, the additional components $f_{xx}^{xy:\text{dis}} = -2f_{yx}^{x^2-y^2:\text{dis}}$, $f_{yx}^{3z^2-r^2:\text{dis}}$, and $f_{zx}^{yz:\text{dis}}$.

Figures 7(a)–7(f) show the color maps of $(\hat{M}_{\alpha,k})_n$ for each band. Focusing first on $(\hat{L}_{z,k})_n$ and $(\hat{S}_{z,k})_n$, we find that the color maps are similar to those of the monolayer MoS₂ [see Figs. 5(c) and 5(f)]. This can be attributed to the fact that the coupling between the in-plane momentum and \hat{M}_z allowed under the C_{3v} is identical to that under the D_{3h} . In the C_{3v} symmetry, coupling terms between \hat{M}_α and \mathbf{k} composed of odd powers of the in-plane momentum $k_{x,y}$ and \hat{M}_z are, in principle, symmetry-allowed. These terms transform as the A_2' representation of D_{3h} . Since \hat{M}_z belongs to A_2' , such terms can emerge only if the odd-momentum polynomial in k_x and k_y transforms as A_1' . However, because the A_1' representation changes sign under mirror operation with respect to the

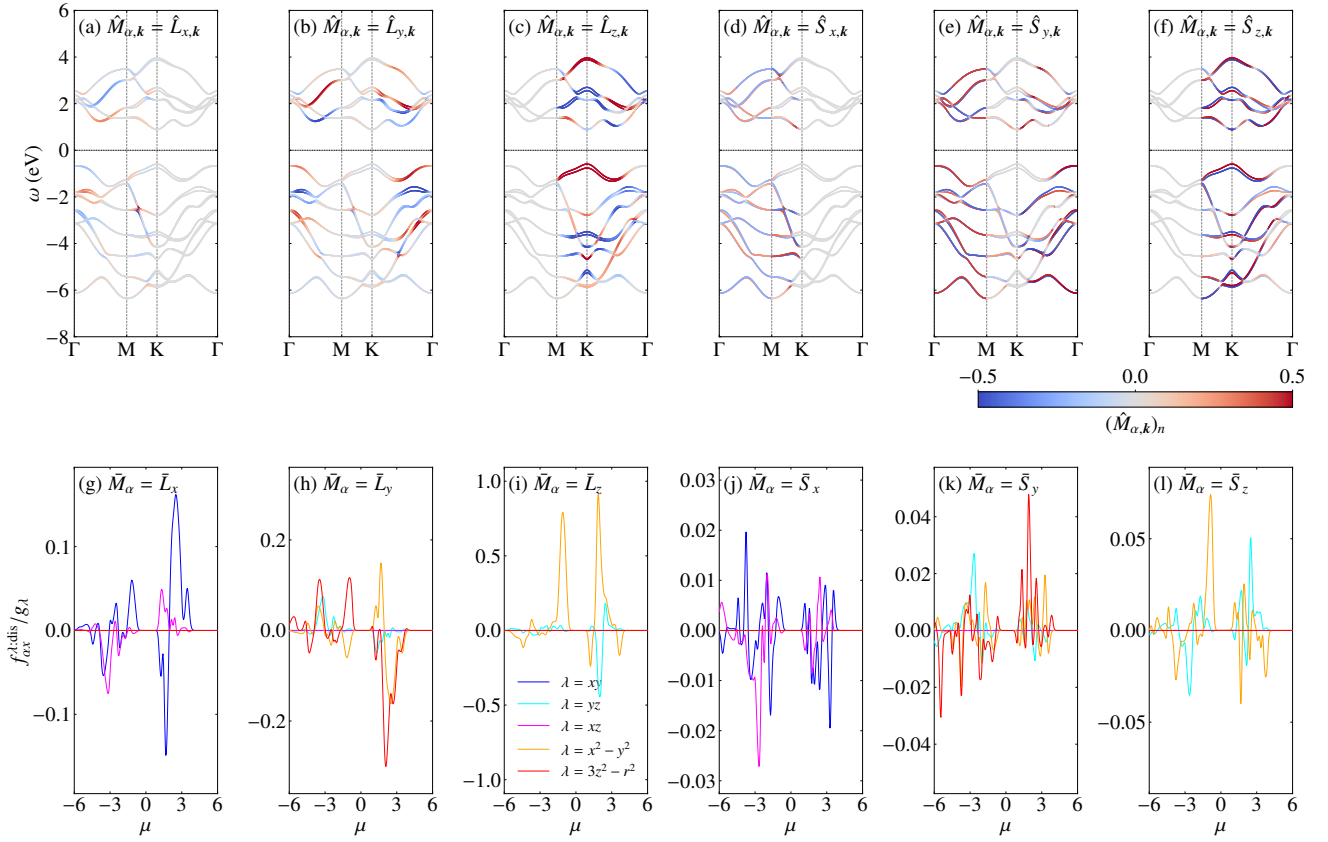


FIG. 7. [(a)–(f)] Band dispersions and color maps of (a) $\langle \hat{L}_{x,k} \rangle_n$, (b) $\langle \hat{L}_{y,k} \rangle_n$, (c) $\langle \hat{L}_{z,k} \rangle_n$, (d) $\langle \hat{S}_{x,k} \rangle_n$, (e) $\langle \hat{S}_{y,k} \rangle_n$, and (f) $\langle \hat{S}_{z,k} \rangle_n$ for monolayer Janus MoSSe. [(g)–(l)] Chemical potential dependence of $f_{\alpha x}^{l:\text{dis}}/g\lambda$ for (g) \bar{L}_x , (h) \bar{L}_y , (i) \bar{L}_z , (j) \bar{S}_x , (k) \bar{S}_y , and (l) \bar{S}_z , with $k_B T = 0.05$ and $\eta = 0.05$. The length of primitive translation vectors is set to 3.251 Å in (g)–(l).

horizontal plane, it cannot be constructed solely from k_x and k_y . Consequently, the symmetry-allowed couplings between \hat{M}_z and the in-plane momentum in C_{3v} are exactly the same as those in D_{3h} . Therefore, the color map structures of $\langle \hat{L}_{z,k} \rangle_n$ and $\langle \hat{S}_{z,k} \rangle_n$ in monolayer MoSSe closely resemble those in monolayer MoS₂. In contrast, as can be seen in Figs. 7(a), 7(b), 7(d), and 7(e), the in-plane components of the magnetization expectations are nonzero in monolayer MoSSe unlike MoS₂. Since $(\hat{M}_y, -\hat{M}_x)$ belongs to the E'' representation, it can be coupled to a basis constructed from odd powers of (k_x, k_y) that belong to E' . At the lowest order, (k_x, k_y) belongs to E' , and thus a Rashba-type term $k_x \hat{M}_y - k_y \hat{M}_x$ is allowed under the C_{3v} symmetry. As a result, the in-plane magnetization expectation values can be finite even in monolayer TMDCs. Indeed, Figs. 7(a) and 7(d) show that along the K– Γ path ($k_y = 0$) the expectation values of $\langle \hat{L}_{x,k} \rangle_n$ and $\langle \hat{S}_{x,k} \rangle_n$ disappear, consistently capturing the characteristic of a Rashba system.

Figures 7(g)–7(l) present the chemical potential dependence of $f_{\alpha x}^{l:\text{dis}}/g\lambda$. As shown in Figs. 7(i) and 7(l), the magnetization response to $\nabla_x \epsilon_{x^2-y^2}$ is nonzero, and its behavior is similar to that of MoS₂. This can be understood from the fact that the color-map patterns of the out-of-plane magnetization expectation values are identical in Figs. 5(f) and 7(f). In contrast to MoS₂, the response to $\nabla_x \epsilon_{yz}$ is also

finite, which is in agreement with the C_{3v} symmetry analysis. For the in-plane magnetization, Figs. 7(g), 7(h), 7(j), and 7(k) show that \bar{M}_x becomes finite in response to $\nabla_x \epsilon_{xy}$ and $\nabla_x \epsilon_{xz}$, and \bar{M}_y becomes finite in response to $\nabla_x \epsilon_{x^2-y^2}$, $\nabla_x \epsilon_{yz}$, and $\nabla_x \epsilon_{3z^2-r^2}$. These results are in full agreement with the symmetry-allowed responses derived above. Moreover, the symmetry argument predicts the relations $f_{xx}^{xz:\text{dis}} = -f_{yx}^{yz:\text{dis}}$ and $f_{xx}^{xy:\text{dis}} = -2f_{yx}^{x^2-y^2:\text{dis}}$. We have confirmed that these relations are satisfied separately for \bar{L} and \bar{S} .

IV. DISCUSSION

In this section, we discuss the experimental detectability of FCIM. We also remark on the limitations of our formulation and possible directions for future extensions.

A. Experimental detectability of FCIM

In time-reversal symmetric metals and semiconductors, FCIM can be experimentally detectable because this effect is the only magnetization response induced by a strain field. When a strain field is applied, the observed magnetization

contains contributions arising from the strain and the strain gradient. Among these, the equilibrium magnetization vanishes in systems with TRS. This can be understood from the fact that strain (and its gradient) and magnetization transform differently under time-reversal operation (see Table I). On the other hand, nonequilibrium magnetization can be induced, which is given by

$$\bar{M}_\alpha = P_\alpha^\lambda \epsilon_\lambda + \int_{\alpha\beta}^{\lambda:\text{dis}} \nabla_\beta \epsilon_\lambda, \quad (47)$$

where $P_\alpha^\lambda = \partial \bar{M}_\alpha / \partial \epsilon_\lambda$ originates from the first term in Eq. (A3). As discussed in Appendix A, the dissipative part of P_α^λ vanishes irrespective of symmetry, and moreover, its nondissipative part also disappears in time-reversal symmetric systems. Therefore, the only magnetization response allowed in systems with TRS is the FCIM for slowly varying strain fields. We expect that nuclear magnetic resonance or magneto-optical Kerr effect can detect the magnetization induced by strain fields.

B. Additional contributions to FCIM

In this study, we have incorporated only the local strain–electric quadrupole coupling. This choice enables a transparent formulation and allows us to elucidate the essential structure of the response in a controlled manner. In realistic crystal systems, however, strain additionally modifies internal microscopic parameters such as hopping amplitudes [53, 54] and the g -tensor [78]. These effects generate effective strain-induced terms in the Hamiltonian. Through these strain-induced modulations of microscopic parameters, the electric quadrupole operators can acquire additional contributions and become nonlocal. These additional terms are expected to generate additional contributions to the FCIM, and taking them into account would provide important quantitative corrections to the present results. Since our formulation remains valid even when $Q_\lambda(\mathbf{r})$ is nonlocal, one can evaluate such additional contributions by directly using Eq. (34).

Furthermore, in our numerical calculations, we have considered only the atomic orbital and spin contributions to the magnetization. However, the orbital magnetic moment of the Bloch electron $U_k^\dagger \hat{L}^{\text{orb}} U_k = -\frac{e}{4} U_k^\dagger (\hat{\mathbf{r}} \times \hat{\mathbf{p}} - \hat{\mathbf{p}} \times \hat{\mathbf{r}}) U_k$ also constitutes an additional source of magnetization [60, 79–85]. Following Refs. [85, 86], its expectation value is given by

$$\begin{aligned} (\hat{L}_{\alpha,k}^{\text{orb}})_n &= (U_k^\dagger \hat{L}_\alpha^{\text{orb}} U_k)_{nm} \\ &= -\epsilon_{\alpha\beta\gamma} \frac{ie}{2\hbar} \left[\frac{\partial U_k^\dagger}{\partial k_\beta} (\hat{H}_k - \epsilon_{k,n}) \frac{\partial U_k}{\partial k_\gamma} \right]_{nm}, \end{aligned} \quad (48)$$

where $\epsilon_{\alpha\beta\gamma}$ is the Levi–Civita symbol. This is a geometric quantity that shares the same transformation properties as the Berry curvature [82, 83]. Consequently, this magnetization vanishes identically in systems that possess spatial inversion and time-reversal symmetries. In the systems considered in this study, spatial inversion symmetry is absent and therefore Eq. (48) can generally take a finite value. A rigorous evaluation of FCIM should incorporate not only the local orbital

and spin magnetization, but also the contribution described by Eq. (48).

C. Extension to insulating systems

We have formulated FCIM in electronic systems and confirmed that a finite response emerges in metals. However, since the electric quadrupole can also be expressed in terms of localized spins [87, 88] or lattice displacements [89, 90], FCIM can also arise in insulating systems through bosonic quasiparticles as elementary excitations (e.g., chiral phonons, magnons, and triplons). In particular, some insulating systems that host bosonic quasiparticles are nonmagnetic [91–93], for which piezomagnetic and flexomagnetic effects are forbidden by TRS. Therefore, in these systems, FCIM is expected to be the only mechanism responsible for magnetization responses induced by strain. Extending the present formalism to insulating systems and quantitatively evaluating the resulting FCIM remain important subjects for future study.

V. SUMMARY

In summary, we have developed a general formalism for the magnetization induced by strain gradients. Starting from free-fermionic systems, we introduced the coupling between strain and electric quadrupoles as an external perturbation and formulated the magnetization response within Kubo’s linear response theory under a spatially varying strain. The resulting response tensor is determined solely by the diagonal components of the electric quadrupole, and this expression is consistent with the one derived from semiclassical theory. Importantly, the FCIM is symmetry-allowed in nonmagnetic systems that preserve TRS, in close analogy with the CIM. A group-theoretical analysis further indicates that FCIM is finite in all 21 noncentrosymmetric point groups in clear contrast to CIM. We have applied the present FCIM formalism to three nonmagnetic tight-binding models: a buckled Lieb lattice, a monolayer MoS₂, and a monolayer Janus MoSSe. These systems lack spatial inversion symmetry, and finite magnetization responses emerge as a consequence of spin-momentum locking, in full agreement with the symmetry-based predictions. In particular, for MoS₂ and MoSSe, the response is strongly enhanced near the band edge, indicating that this effect should be experimentally observable.

ACKNOWLEDGMENTS

The authors thank S. Hayami and Y. Miyata for fruitful discussions. This work was supported by Grant-in-Aid for Scientific Research from JSPS, KAKENHI Grant Nos. JP23H04866 and JP23H04869.

Appendix A: Expression of $f_{\alpha\beta}^{\lambda(2)}$

In this section, we show the derivation of Eq (31) in detail. We denote the second term of Eq. (28) as $\bar{M}_\alpha^{(2)}$, which is given by

$$\bar{M}_\alpha^{(2)} = -\frac{1}{V} \sum_{\lambda}^{\text{Irrep.}} g_\lambda \int dt e^{-\delta t} \int_0^{\frac{1}{k_B T}} d\beta' \int d\mathbf{r} \int d\mathbf{r}' \langle \tau^\lambda(\mathbf{r}, -i\hbar\beta') M_\alpha(\mathbf{r}', t) \rangle_{\text{eq}} \epsilon_\lambda(\mathbf{r}). \quad (\text{A1})$$

We assume that the response at \mathbf{r}' is primarily influenced by the strain gradient in its immediate vicinity and expand $\epsilon_\lambda(\mathbf{r})$ around \mathbf{r}' , corresponding to a long-wavelength expansion. Then, $\epsilon_\lambda(\mathbf{r})$ can be written as

$$\epsilon_\lambda(\mathbf{r}) = \epsilon_\lambda(\mathbf{r}') + \nabla \epsilon_\lambda(\mathbf{r}) \Big|_{\mathbf{r}=\mathbf{r}'} \cdot (\mathbf{r} - \mathbf{r}') + \dots \quad (\text{A2})$$

Substituting this expansion into Eq. (A1) yields

$$\begin{aligned} \bar{M}_\alpha^{(2)} = & -\frac{1}{V} \sum_{\lambda}^{\text{Irrep.}} g_\lambda \int dt e^{-\delta t} \int_0^{\frac{1}{k_B T}} d\beta' \int d\mathbf{r} \int d\mathbf{r}' \langle \tau^\lambda(\mathbf{r}, -i\hbar\beta') M_\alpha(\mathbf{r}', t) \rangle_{\text{eq}} \epsilon_\lambda(\mathbf{r}') \\ & - \frac{1}{V} \sum_{\lambda}^{\text{Irrep.}} g_\lambda \int dt e^{-\delta t} \int_0^{\frac{1}{k_B T}} d\beta' \left[\frac{\partial}{\partial i\mathbf{q}} \langle \tau_{-q}^\lambda(-i\hbar\beta') M_{\alpha,q}(t) \rangle_{\text{eq}} \Big|_{q=0} \right] \cdot \nabla \epsilon_\lambda, \end{aligned} \quad (\text{A3})$$

where we have used

$$\int d\mathbf{r} \int d\mathbf{r}' \langle \tau^\lambda(\mathbf{r}, -i\hbar\beta') M_\alpha(\mathbf{r}', t) \rangle_{\text{eq}} (\mathbf{r} - \mathbf{r}') = \frac{\partial}{\partial i\mathbf{q}} \langle \tau_{-q}^\lambda(-i\hbar\beta') M_{\alpha,q}(t) \rangle_{\text{eq}} \Big|_{q=0}. \quad (\text{A4})$$

By defining $f_{\alpha\beta}^{\lambda(2)} = \partial \bar{M}_\alpha^{(2)} / \partial (\nabla_\beta \epsilon_\lambda)$, we obtain Eq. (31).

We comment on the first term in Eq. (A3). This term represents the magnetization induced by the strain, indicating that the strain itself can generate a finite magnetization. $P_\alpha^\lambda = \partial \bar{M}_\alpha / \partial \epsilon_\lambda$ in Eq. (47) corresponds to the first term in Eq. (A3). P_α^λ contains both dissipative and nondissipative contributions. Evaluating the dissipative part following Appendix B, we find that it depends on $(\hat{\tau}_k^\lambda)_n$. Since $(\hat{\tau}_k^\lambda)_n = 0$ for all bands, the dissipative contribution vanishes. In contrast, the nondissipative contribution depends on $(\hat{\tau}_k^\lambda)_{nm}$ with $n \neq m$ and is in general nonzero. However, in systems with TRS, this contribution vanishes. This can be understood from the fact that the nondissipative part transform as $M_\alpha \epsilon_\lambda$. According to Table I, $M_\alpha \epsilon_\lambda$ is odd under time-reversal operation. Therefore, P_α^λ vanishes in time-reversal symmetric systems.

Appendix B: Derivation of $f_{\alpha\beta}^{\lambda:\text{dis}}$

In this section, we derive the explicit expressions for $f_{\alpha\beta}^{\lambda:\text{dis}} = f_{\alpha\beta}^{\lambda(1):\text{dis}} + f_{\alpha\beta}^{\lambda(2):\text{dis}}$.

First, evaluating $f_{\alpha\beta}^{\lambda(1)}$ in Eq. (30), we find

$$f_{\alpha\beta}^{\lambda(1)} = \frac{i\hbar g_\lambda}{V} \sum_k \sum_{nm=1}^N \frac{f(\epsilon_{k,n}) - f(\epsilon_{k,m})}{\epsilon_{k,n} - \epsilon_{k,m}} \frac{(\hat{M}_{\alpha,k})_{nm} (\hat{J}_{\beta,k}^\lambda)_{mn}}{\epsilon_{k,n} - \epsilon_{k,m} + i\delta}. \quad (\text{B1})$$

To take into account nonmagnetic impurity scattering at low temperatures phenomenologically, we introduce a small but finite positive η and replace $i\delta$ with $i\eta$. Using the relation $\text{Im} \frac{1}{x+i\eta} = -\frac{\eta}{x^2+\eta^2}$, the dissipative part of $f_{\alpha\beta}^{\lambda(1)}$ is expressed as

$$\begin{aligned} f_{\alpha\beta}^{\lambda(1):\text{dis}} &= \frac{\hbar g_\lambda}{V} \sum_k \sum_{nm=1}^N \frac{f(\epsilon_{k,n}) - f(\epsilon_{k,m})}{\epsilon_{k,n} - \epsilon_{k,m}} (\hat{M}_{\alpha,k})_{nm} (\hat{J}_{\beta,k}^\lambda)_{mn} \frac{\eta}{(\epsilon_{k,n} - \epsilon_{k,m})^2 + \eta^2} \\ &= \frac{\hbar g_\lambda}{V\eta} \sum_k \sum_{n=1}^N (\hat{M}_{\alpha,k})_n (\hat{J}_{\beta,k}^\lambda)_n \frac{\partial f(\epsilon_{k,n})}{\partial \epsilon_{k,n}}, \end{aligned} \quad (\text{B2})$$

where we use $\frac{f(\varepsilon_{k,n})-f(\varepsilon_{k,m})}{\varepsilon_{k,n}-\varepsilon_{k,m}} \rightarrow \frac{\partial f(\varepsilon_{k,n})}{\partial \varepsilon_{k,n}}$ for $\varepsilon_{k,m} \sim \varepsilon_{k,n}$. Strictly speaking, Eq. (B2) also contains a finite interband contribution for small but finite η . We have kept only the intraband contribution that diverges as $1/\eta$ in the limit $\eta \rightarrow 0$ and neglected the interband contribution, which vanishes as $O(\eta)$. This expression coincides with Eq. (32).

Next, we evaluate $f_{\alpha\beta}^{\lambda(2)}$ given in Eq. (31), which can be written as follows:

$$\begin{aligned} f_{\alpha\beta}^{\lambda(2)} &= -\frac{g\lambda}{V} \int dt e^{-\delta t} \int_0^{\frac{1}{k_{\text{B}}T}} ds \left[\frac{\partial}{\partial i q_{\beta}} \langle \tau_{-q}^{\lambda}(-i\hbar s) M_{\alpha,q}(t) \rangle_{\text{eq}} \Big|_{q=0} \right] \\ &= -\frac{g\lambda}{V} \int dt e^{-\delta t} \int_0^{\frac{1}{k_{\text{B}}T}} ds \int d\mathbf{r} \int d\mathbf{r}' \left[r_{\beta} \langle \tau^{\lambda}(\mathbf{r}, -i\hbar s) M_{\alpha}(\mathbf{r}', t) \rangle_{\text{eq}} - r'_{\beta} \langle \tau^{\lambda}(\mathbf{r}, -i\hbar s) M_{\alpha}(\mathbf{r}', t) \rangle_{\text{eq}} \right] \\ &= -\frac{g\lambda}{V} \int dt e^{-\delta t} \int_0^{\frac{1}{k_{\text{B}}T}} ds \left[\langle D_{\beta}^{\tau^{\lambda}}(-i\hbar s) M_{\alpha,q=0}(t) \rangle_{\text{eq}} - \langle \tau_{-q=0}^{\lambda}(-i\hbar s) D_{\beta}^{M_{\alpha}}(t) \rangle_{\text{eq}} \right], \end{aligned} \quad (\text{B3})$$

where we introduce $\mathbf{D}^{\tau^{\lambda}} = \int \mathbf{r} \tau^{\lambda}(\mathbf{r}) d\mathbf{r}$ and $\mathbf{D}^{M_{\alpha}} = \int \mathbf{r}' M_{\alpha}(\mathbf{r}') d\mathbf{r}'$. To facilitate the calculation in momentum space, it is useful to rewrite these operators in the following forms. Using Eqs. (21) and (26), we obtain

$$\begin{aligned} \mathbf{D}^{\tau^{\lambda}} &= \frac{1}{2} \int \left\{ [\hat{\mathbf{r}}\Psi(\mathbf{r})]^{\dagger} \hat{\tau}^{\lambda} \Psi(\mathbf{r}) + [\hat{\tau}^{\lambda} \Psi(\mathbf{r})]^{\dagger} \hat{\mathbf{r}} \Psi(\mathbf{r}) \right\} d\mathbf{r} \\ &= \frac{1}{2} \int \Psi^{\dagger}(\mathbf{r}) (\hat{\mathbf{r}} \hat{\tau}^{\lambda} + \hat{\tau}^{\lambda} \hat{\mathbf{r}}) \Psi(\mathbf{r}) d\mathbf{r}, \end{aligned} \quad (\text{B4})$$

$$\begin{aligned} \mathbf{D}^{M_{\alpha}} &= \frac{1}{2} \int \left\{ [\hat{\mathbf{r}}\Psi(\mathbf{r}')]^{\dagger} \hat{M}_{\alpha} \Psi(\mathbf{r}') + [\hat{M}_{\alpha} \Psi(\mathbf{r}')]^{\dagger} \hat{\mathbf{r}} \Psi(\mathbf{r}') \right\} d\mathbf{r}' \\ &= \frac{1}{2} \int \Psi^{\dagger}(\mathbf{r}') (\hat{\mathbf{r}} \hat{M}_{\alpha} + \hat{M}_{\alpha} \hat{\mathbf{r}}) \Psi(\mathbf{r}') d\mathbf{r}', \end{aligned} \quad (\text{B5})$$

where we have used $\hat{\tau}^{\lambda} = (\hat{\tau}^{\lambda})^{\dagger}$, $\hat{M}_{\alpha} = \hat{M}_{\alpha}^{\dagger}$, and $\Psi^{\dagger}(\mathbf{r}') \hat{M}_{\alpha} \Psi(\mathbf{r}') = [\hat{M}_{\alpha} \Psi(\mathbf{r}')]^{\dagger} \Psi(\mathbf{r}')$. Applying Eq. (2) to Eq. (B3) and employing the Bloch basis, we find

$$\begin{aligned} f_{\alpha\beta}^{\lambda(2)} &= \frac{i\hbar g\lambda}{2V} \sum_{\mathbf{k}} \sum_{nm=1}^N \frac{f(\varepsilon_{k,n}) - f(\varepsilon_{k,m})}{\varepsilon_{k,n} - \varepsilon_{k,m}} \frac{1}{\varepsilon_{k,n} - \varepsilon_{k,m} + i\delta} \left[(\hat{M}_{\alpha,k})_{nm} (\hat{r}_{\beta} \hat{\tau}_k^{\lambda} + \hat{\tau}_k^{\lambda} \hat{r}_{\beta})_{mn} - (\hat{r}_{\beta} \hat{M}_{\alpha,k} + \hat{M}_{\alpha,k} \hat{r}_{\beta})_{nm} (\hat{\tau}_k^{\lambda})_{mn} \right] \\ &= \frac{i\hbar g\lambda}{2V} \sum_{\mathbf{k}} \sum_{nm=1}^N \frac{f(\varepsilon_{k,n}) - f(\varepsilon_{k,m})}{\varepsilon_{k,n} - \varepsilon_{k,m}} \frac{1}{\varepsilon_{k,n} - \varepsilon_{k,m} + i\delta} \left\{ (\hat{M}_{\alpha,k})_{nm} \left[\sum_{l(\neq m)}^N (\hat{r}_{\beta})_{ml} (\hat{\tau}_k^{\lambda})_{ln} + \sum_{l(\neq n)}^N (\hat{\tau}_k^{\lambda})_{ml} (\hat{r}_{\beta})_{ln} \right] \right. \\ &\quad \left. - \left[\sum_{l(\neq n)}^N (\hat{r}_{\beta})_{nl} (\hat{M}_{\alpha,k})_{lm} + \sum_{l(\neq m)}^N (\hat{M}_{\alpha,k})_{nl} (\hat{r}_{\beta})_{lm} \right] (\hat{\tau}_k^{\lambda})_{mn} \right\}, \end{aligned} \quad (\text{B6})$$

where the contribution from the diagonal elements of \hat{r}_{β} cancels out. Using $(\hat{r}_{\beta})_{nm} = (A_{\mathbf{k}}^{\beta})_{nm}$ for $n \neq m$ [94, 95], where $(A_{\mathbf{k}}^{\beta})_{nm}$ is the interband Berry connection defined as

$$(A_{\mathbf{k}}^{\beta})_{nm} = i \left(U_{\mathbf{k}}^{\dagger} \frac{\partial U_{\mathbf{k}}}{\partial k_{\beta}} \right)_{nm}, \quad (\text{B7})$$

$f_{\alpha\beta}^{\lambda(2)}$ can be expressed as

$$\begin{aligned} f_{\alpha\beta}^{\lambda(2)} &= \frac{i\hbar g\lambda}{2V} \sum_{\mathbf{k}} \sum_{nm=1}^N \frac{f(\varepsilon_{k,n}) - f(\varepsilon_{k,m})}{\varepsilon_{k,n} - \varepsilon_{k,m}} \frac{1}{\varepsilon_{k,n} - \varepsilon_{k,m} + i\delta} \left\{ (\hat{M}_{\alpha,k})_{nm} \left[\sum_{l(\neq m)}^N (A_{\mathbf{k}}^{\beta})_{ml} (\hat{\tau}_k^{\lambda})_{ln} + \sum_{l(\neq n)}^N (\hat{\tau}_k^{\lambda})_{ml} (A_{\mathbf{k}}^{\beta})_{ln} \right] \right. \\ &\quad \left. - \left[\sum_{l(\neq n)}^N (A_{\mathbf{k}}^{\beta})_{nl} (\hat{M}_{\alpha,k})_{lm} + \sum_{l(\neq m)}^N (\hat{M}_{\alpha,k})_{nl} (A_{\mathbf{k}}^{\beta})_{lm} \right] (\hat{\tau}_k^{\lambda})_{mn} \right\} \\ &= \frac{i\hbar g\lambda}{2V} \sum_{\mathbf{k}} \sum_{nm=1}^N \frac{f(\varepsilon_{k,n}) - f(\varepsilon_{k,m})}{\varepsilon_{k,n} - \varepsilon_{k,m}} \frac{1}{\varepsilon_{k,n} - \varepsilon_{k,m} + i\delta} \left\{ (\hat{M}_{\alpha,k})_{nm} \left[\sum_{l(\neq m)}^N \frac{\varepsilon_{k,l} - \varepsilon_{k,n}}{\varepsilon_{k,m} - \varepsilon_{k,l}} (\hat{v}_{\beta,k})_{ml} (\hat{Q}_{\lambda,k})_{ln} + \sum_{l(\neq n)}^N \frac{\varepsilon_{k,m} - \varepsilon_{k,l}}{\varepsilon_{k,l} - \varepsilon_{k,n}} (\hat{Q}_{\lambda,k})_{ml} (\hat{v}_{\beta,k})_{ln} \right] \right. \\ &\quad \left. - \left[\sum_{l(\neq n)}^N \frac{\varepsilon_{k,m} - \varepsilon_{k,n}}{\varepsilon_{k,n} - \varepsilon_{k,l}} (\hat{v}_{\beta,k})_{nl} (\hat{M}_{\alpha,k})_{lm} + \sum_{l(\neq m)}^N \frac{\varepsilon_{k,m} - \varepsilon_{k,n}}{\varepsilon_{k,l} - \varepsilon_{k,m}} (\hat{M}_{\alpha,k})_{nl} (\hat{v}_{\beta,k})_{lm} \right] (\hat{Q}_{\lambda,k})_{mn} \right\}. \end{aligned} \quad (\text{B8})$$

Here, we have used the following relations:

$$(A_{\mathbf{k}}^{\beta})_{nm} = -i\hbar \frac{(\hat{v}_{\beta,\mathbf{k}})_{nm}}{\varepsilon_{\mathbf{k},n} - \varepsilon_{\mathbf{k},m}}, \quad (n \neq m), \quad (\text{B9})$$

$$(\hat{\tau}_{\mathbf{k}})_{nm} = \frac{i}{\hbar} (\varepsilon_{\mathbf{k},n} - \varepsilon_{\mathbf{k},m}) (\hat{Q}_{\lambda,\mathbf{k}})_{nm}. \quad (\text{B10})$$

Similarly to the derivation of $f_{\alpha\beta}^{\lambda(1):\text{dis}}$, the dissipative part of $f_{\alpha\beta}^{\lambda(2)}$ is obtained as

$$\begin{aligned} f_{\alpha\beta}^{\lambda(2):\text{dis}} &= \frac{\hbar g_{\lambda}}{2V\eta} \sum_{\mathbf{k}} \sum_{n=1}^N \sum_{l(\neq n)}^N (\hat{M}_{\alpha,\mathbf{k}})_n \left[-(\hat{v}_{\beta,\mathbf{k}})_{nl} (\hat{Q}_{\lambda,\mathbf{k}})_{ln} - (\hat{Q}_{\lambda,\mathbf{k}})_{nl} (\hat{v}_{\beta,\mathbf{k}})_{ln} \right] \frac{\partial f(\varepsilon_{\mathbf{k},n})}{\partial \varepsilon_{\mathbf{k},n}} \\ &= -\frac{\hbar g_{\lambda}}{V\eta} \sum_{\mathbf{k}} \sum_{n=1}^N \sum_{l(\neq n)}^N (\hat{M}_{\alpha,\mathbf{k}})_n \text{Re} \left[(\hat{v}_{\beta,\mathbf{k}})_{nl} (\hat{Q}_{\lambda,\mathbf{k}})_{ln} \right] \frac{\partial f(\varepsilon_{\mathbf{k},n})}{\partial \varepsilon_{\mathbf{k},n}}. \end{aligned} \quad (\text{B11})$$

This expression corresponds to Eq. (33).

Appendix C: Electric quadrupole operators in monolayer MoS₂

We list the expressions of electric quadrupole operators for the d electrons in MoS₂. We denote by $d_{i,\lambda\sigma}^{\dagger}$ and $d_{i,\lambda\sigma}$ the creation and annihilation operators, respectively, for the d -orbitals on the Mo atom in unit cell i . The corresponding quadrupole operators in unit cell i are given by

$$Q_{i,x^2-y^2} = \frac{1}{\sqrt{7}} \sum_{\sigma} \left[-(2d_{i,3z^2-r^2\sigma}^{\dagger} d_{i,x^2-y^2\sigma} + \text{H.c.}) - \sqrt{3}d_{i,yz\sigma}^{\dagger} d_{i,yz\sigma} + \sqrt{3}d_{i,xz\sigma}^{\dagger} d_{i,xz\sigma} \right], \quad (\text{C1})$$

$$Q_{i,3z^2-r^2} = \frac{1}{\sqrt{7}} \sum_{\sigma} \left(2d_{i,3z^2-r^2\sigma}^{\dagger} d_{i,3z^2-r^2\sigma} - 2d_{i,x^2-y^2\sigma}^{\dagger} d_{i,x^2-y^2\sigma} + d_{i,yz\sigma}^{\dagger} d_{i,yz\sigma} + d_{i,xz\sigma}^{\dagger} d_{i,xz\sigma} - 2d_{i,xy\sigma}^{\dagger} d_{i,xy\sigma} \right), \quad (\text{C2})$$

$$Q_{i,xy} = \frac{1}{\sqrt{7}} \sum_{\sigma} \left(-2d_{i,3z^2-r^2\sigma}^{\dagger} d_{i,xy\sigma} + \sqrt{3}d_{i,yz\sigma}^{\dagger} d_{i,xz\sigma} + \text{H.c.} \right), \quad (\text{C3})$$

$$Q_{i,yz} = \frac{1}{\sqrt{7}} \sum_{\sigma} \left(d_{i,3z^2-r^2\sigma}^{\dagger} d_{i,yz\sigma} - \sqrt{3}d_{i,x^2-y^2\sigma}^{\dagger} d_{i,yz\sigma} + \sqrt{3}d_{i,xz\sigma}^{\dagger} d_{i,xy\sigma} + \text{H.c.} \right), \quad (\text{C4})$$

$$Q_{i,xz} = \frac{1}{\sqrt{7}} \sum_{\sigma} \left(d_{i,3z^2-r^2\sigma}^{\dagger} d_{i,xz\sigma} + \sqrt{3}d_{i,x^2-y^2\sigma}^{\dagger} d_{i,xz\sigma} + \sqrt{3}d_{i,yz\sigma}^{\dagger} d_{i,xy\sigma} + \text{H.c.} \right). \quad (\text{C5})$$

-
- [1] N. A. Spaldin and M. Fiebig, The Renaissance of Magnetoelectric Multiferroics, *Science* **309**, 391 (2005).
 - [2] V. J. Folen, G. T. Rado, and E. W. Stalder, Anisotropy of the Magnetoelectric Effect in Cr₂O₃, *Phys. Rev. Lett.* **6**, 607 (1961).
 - [3] S.-W. Cheong and M. Mostovoy, Multiferroics: a magnetic twist for ferroelectricity, *Nat. Mater.* **6**, 13 (2007).
 - [4] Y. Tokura, S. Seki, and N. Nagaosa, Multiferroics of spin origin, *Rep. Prog. Phys.* **77**, 076501 (2014).
 - [5] W. Eerenstein, N. Mathur, and J. Scott, Multiferroic and magnetoelectric materials, *Nature* **442**, 759 (2006).
 - [6] D. Khomskii, Classifying multiferroics: Mechanisms and effects, *Physics* **2**, 20 (2009).
 - [7] N. A. Spaldin, M. Fiebig, and M. Mostovoy, The toroidal moment in condensed-matter physics and its relation to the magnetoelectric effect*, *J. Phys.: Condens. Matter* **20**, 434203 (2008).
 - [8] A. Zimmermann, D. Meier, and M. Fiebig, Ferroic nature of magnetic toroidal order, *Nat. Commun.* **5**, 4796 (2014).
 - [9] L. D. Landau and E. M. Lifshitz, *Statistical Physics* (Pergamon Press, Oxford, 1980).
 - [10] S. Hayami, M. Yatsushiro, Y. Yanagi, and H. Kusunose, Classification of atomic-scale multipoles under crystallographic point groups and application to linear response tensors, *Phys. Rev. B* **98**, 165110 (2018).
 - [11] M. Yatsushiro, H. Kusunose, and S. Hayami, Multipole classification in 122 magnetic point groups for unified understanding of multiferroic responses and transport phenomena, *Phys. Rev. B* **104**, 054412 (2021).
 - [12] Y. Kuramoto, H. Kusunose, and A. Kiss, Multipole Orders and Fluctuations in Strongly Correlated Electron Systems, *J. Phys. Soc. Jpn.* **78**, 072001 (2009).

- [13] M.-T. Suzuki, H. Ikeda, and P. M. Oppeneer, First-principles Theory of Magnetic Multipoles in Condensed Matter Systems, *J. Phys. Soc. Jpn.* **87**, 041008 (2018).
- [14] M. Bibes and A. Barthélemy, Towards a magnetoelectric memory, *Nat. Mater.* **7**, 425 (2008).
- [15] F. Narita and M. Fox, A Review on Piezoelectric, Magnetostrictive, and Magnetoelectric Materials and Device Technologies for Energy Harvesting Applications, *Adv. Eng. Mater.* **20**, 1700743 (2018).
- [16] C. R. Bowen, H. A. Kim, P. M. Weaver, and S. Dunn, Piezoelectric and ferroelectric materials and structures for energy harvesting applications, *Energy Environ. Sci.* **7**, 25 (2014).
- [17] A. A. Bukharaev, A. K. Zvezdin, A. P. Pyatakov, and Y. K. Fetisov, Straintronics: a new trend in micro- and nanoelectronics and materials science, *Physics-Uspokhi* **61**, 1175 (2018).
- [18] A. Manchon, J. Železný, I. M. Miron, T. Jungwirth, J. Sinova, A. Thiaville, K. Garello, and P. Gambardella, Current-induced spin-orbit torques in ferromagnetic and antiferromagnetic systems, *Rev. Mod. Phys.* **91**, 035004 (2019).
- [19] A. Hirohata, K. Yamada, Y. Nakatani, I.-L. Prejbeanu, B. Diény, P. Pirro, and B. Hillebrands, Review on spintronics: Principles and device applications, *J. Magn. Magn. Mater.* **509**, 166711 (2020).
- [20] A. Fert, R. Ramesh, V. Garcia, F. Casanova, and M. Bibes, Electrical control of magnetism by electric field and current-induced torques, *Rev. Mod. Phys.* **96**, 015005 (2024).
- [21] P. Curie, Sur la symétrie dans les phénomènes physiques, symétrie d'un champ électrique et d'un champ magnétique, *J. Phys. Theor. Appl.* **3**, 393 (1894).
- [22] I. E. Dzyaloshinskii, On the magneto-electrical effects in antiferromagnets, *Sov. Phys. JETP* **10**, 628 (1960).
- [23] T. H. O'Dell, The electro-dynamics of magneto-electric media, *Philos. Mag.-J. Theor. Exp. Appl. Phys.* **7**, 1653 (1962).
- [24] S. Dong, H. Xiang, and E. Dagotto, Magnetoelectricity in multiferroics: a theoretical perspective, *Natl. Sci. Rev.* **6**, 629 (2019).
- [25] B. A. Tavger and V. M. Zaitsev, Magnetic symmetry of crystals, *Sov. Phys. JETP* **3**, 430 (1956).
- [26] M. Dyakonov and V. Perel, Current-induced spin orientation of electrons in semiconductors, *Physics Letters A* **35**, 459 (1971).
- [27] E. L. Ivchenko and G. E. Pikus, New photogalvanic effect in gyrotropic crystals, *JETP Lett.* **27**, 604 (1978).
- [28] V. Edelstein, Spin polarization of conduction electrons induced by electric current in two-dimensional asymmetric electron systems, *Solid State Commun.* **73**, 233 (1990).
- [29] J. Sánchez, L. Vila, G. Desfonds, S. Gambarelli, J. Attané, J. D. Teresa, C. Magén, and A. Fert, Spin-to-charge conversion using Rashba coupling at the interface between non-magnetic materials, *Nat. Commun.* **4**, 2944 (2013).
- [30] E. A. Eliseev, A. N. Morozovska, M. D. Glinchuk, and R. Blinc, Spontaneous flexoelectric/flexomagnetic effect in nanoferroics, *Phys. Rev. B* **79**, 165433 (2009).
- [31] P. Lukashev and R. F. Sabirianov, Flexomagnetic effect in frustrated triangular magnetic structures, *Phys. Rev. B* **82**, 094417 (2010).
- [32] Z. Tang, Q. Gong, and M. Yi, Flexomagnetism: Progress, challenges, and opportunities, *Mater. Sci. Eng. R* **162**, 100878 (2025).
- [33] L. Shu, R. Liang, Z. Rao, L. Fei, S. Ke, and Y. Wang, Flexoelectric materials and their related applications: A focused review, *J. Adv. Ceram.* **8**, 153 (2019).
- [34] C. Chappert, A. Fert, and F. V. Dau, The emergence of spin electronics in data storage, *Nat. Mater.* **6**, 813 (2007).
- [35] E. A. Eliseev, M. D. Glinchuk, V. Khist, V. V. Skorokhod, R. Blinc, and A. N. Morozovska, Linear magnetoelectric coupling and ferroelectricity induced by the flexomagnetic effect in ferroics, *Phys. Rev. B* **84**, 174112 (2011).
- [36] W. Shi, Y. Guo, Z. Zhang, and W. Guo, Strain Gradient Mediated Magnetism and Polarization in Monolayer VSe₂, *J. Phys. Chem. C* **123**, 24988 (2019).
- [37] A. Edström, D. Amoroso, S. Picozzi, P. Barone, and M. Stengel, Curved Magnetism in CrI₃, *Phys. Rev. Lett.* **128**, 177202 (2022).
- [38] G. Qiu, Z. Li, K. Zhou, and Y. Cai, Flexomagnetic noncollinear state with a plumb line shape spin configuration in edged two-dimensional magnetic CrI₃, *npj Quantum Mater.* **8**, 15 (2023).
- [39] L. Qiao, J. Sladek, V. Sladek, A. S. Kaminskiy, A. P. Pyatakov, and W. Ren, Curvature-induced magnetization in a CrI₃ bilayer: Flexomagnetic effect enhancement in van der Waals antiferromagnets, *Phys. Rev. B* **109**, 014410 (2024).
- [40] Z. Tang, Q. Gong, and M. Yi, Intrinsic flexomagnetism of antiferromagnetic monolayer FeSe, *Phys. Rev. B* **112**, 014432 (2025).
- [41] Y. Liu, W. Chen, Y. Yin, Z. Tang, Q. Gong, M. Yi, and Y. Liu, Large piezo-/flexo-electric and flexomagnetic effects in a semiconducting cobalt telluride monolayer, *Nanoscale Horiz.* **10**, 2995 (2025).
- [42] Y.-H. Shen, Y.-X. Song, W.-Y. Tong, X.-W. Shen, S.-j. Gong, and C.-G. Duan, Giant Flexomagnetolectric Effect in Dilute Magnetic Monolayer, *Adv. Theor. Simul.* **1**, 1800048 (2018).
- [43] B. A. Belyaev, A. V. Izotov, P. N. Solovov, and N. M. Boev, Strain-Gradient-Induced Unidirectional Magnetic Anisotropy in Nanocrystalline Thin Permalloy Films, *Phys. Status Solidi RRL* **14**, 1900467 (2020).
- [44] Y. Ling, X. Yu, S. Yuan, A. He, Z. Han, J. Du, Q. Fan, S. Yan, and Q. Xu, Flexomagnetic Effect Enhanced Ferromagnetism and Magnetochemistry in Freestanding High-Entropy Alloy Films, *ACS Nano* **17**, 17299 (2023), doi: 10.1021/acsnano.3c05255.
- [45] P. Makushko, T. Kosub, O. Pylypovskiy, N. Hedrich, J. Li, A. Pashkin, S. Avdoshenko, R. Hübner, F. Ganss, D. Wolf, A. Lubk, M. Liedke, M. Butterling, A. Wagner, K. Wagner, B. Shields, P. Lehmann, I. Veremchuk, J. Fassbender, P. Maletinsky, and D. Makarov, Flexomagnetism and vertically graded Néel temperature of antiferromagnetic Cr₂O₃ thin films, *Nat. Commun.* **13**, 6745 (2022).
- [46] E. R. Callen and H. B. Callen, Static Magnetoelastic Coupling in Cubic Crystals, *Phys. Rev.* **129**, 578 (1963).
- [47] E. Callen and H. B. Callen, Magnetostriction, Forced Magnetostriction, and Anomalous Thermal Expansion in Ferromagnets, *Phys. Rev.* **139**, A455 (1965).
- [48] S. Ji, C. Song, J. Koo, J. Park, Y. J. Park, K.-B. Lee, S. Lee, J.-G. Park, J. Y. Kim, B. K. Cho, K.-P. Hong, C.-H. Lee, and F. Iga, Resonant X-Ray Scattering Study of Quadrupole-Strain Coupling in DyB₄, *Phys. Rev. Lett.* **99**, 076401 (2007).
- [49] E. W. Rosenberg, J.-H. Chu, J. P. C. Ruff, A. T. Hristov, and I. R. Fisher, Divergence of the quadrupole-strain susceptibility of the electronic nematic system YbRu₂Ge₂, *Proc. Natl. Acad. Sci. U.S.A.* **116**, 7232 (2019).
- [50] J. M. Luttinger, Theory of Thermal Transport Coefficients, *Phys. Rev.* **135**, A1505 (1964).
- [51] R. Kubo, M. Yokota, and S. Nakajima, Statistical-Mechanical Theory of Irreversible Processes. II. Response to Thermal Disturbance, *J. Phys. Soc. Jpn.* **12**, 1203 (1957).
- [52] The definition of $Q_\lambda(\mathbf{r})$ is fixed by the requirement that the Hamiltonian be Hermitian. When modulation of hopping amplitudes is taken into account, \hat{Q}_λ can generally become a non-local operator. Nevertheless, as long as $Q_\lambda(\mathbf{r}) = Q_\lambda^\dagger(\mathbf{r})$ [Eq. (9)] is satisfied, \mathcal{V} is guaranteed to be Hermitian, and the formula-

- tion in the present study remains valid even if \hat{Q}_l is a non-local operator. A similar definition of a local density can also be found in Eq. (21) of Ref. [96].
- [53] Y. Ogawa, T. Funato, and H. Kohno, Microscopic Analysis of Lattice Distortion Effects in Rashba Systems, *J. Phys. Soc. Jpn.* **92**, 113702 (2023).
- [54] K. Uchino, Y. Ogawa, and S. Hayami, Analysis of Spin Current Generation by Elastic Waves in f -wave Altermagnets, [arXiv:2508.06027](https://arxiv.org/abs/2508.06027).
- [55] M.-C. Chang and Q. Niu, Berry phase, hyperorbits, and the Hofstadter spectrum: Semiclassical dynamics in magnetic Bloch bands, *Phys. Rev. B* **53**, 7010 (1996).
- [56] G. Sundaram and Q. Niu, Wave-packet dynamics in slowly perturbed crystals: Gradient corrections and Berry-phase effects, *Phys. Rev. B* **59**, 14915 (1999).
- [57] L. Dong, C. Xiao, B. Xiong, and Q. Niu, Berry Phase Effects in Dipole Density and the Mott Relation, *Phys. Rev. Lett.* **124**, 066601 (2020).
- [58] F. Freimuth, S. Blügel, and Y. Mokrousov, Spin-orbit torques in Co/Pt(111) and Mn/W(001) magnetic bilayers from first principles, *Phys. Rev. B* **90**, 174423 (2014).
- [59] J. Železný, Y. Zhang, C. Felser, and B. Yan, Spin-Polarized Current in Noncollinear Antiferromagnets, *Phys. Rev. Lett.* **119**, 187204 (2017).
- [60] A. Johansson, Theory of spin and orbital Edelstein effects, *J. Phys.: Condens. Matter* **36**, 423002 (2024).
- [61] D. M. Juraschek, M. Fechner, A. V. Balatsky, and N. A. Spaldin, Dynamical multiferroicity, *Phys. Rev. Mater.* **1**, 014401 (2017).
- [62] D. M. Juraschek and N. A. Spaldin, Orbital magnetic moments of phonons, *Phys. Rev. Mater.* **3**, 064405 (2019).
- [63] P. C. Lou, A. Kataliha, R. G. Bhardwaj, W. P. Beyermann, D. M. Juraschek, and S. Kumar, Large Magnetic Moment in Flexoelectronic Silicon at Room Temperature, *Nano Lett.* **21**, 2939 (2021).
- [64] S. Fang, R. Kuate Defo, S. N. Shirodkar, S. Lieu, G. A. Tritsaris, and E. Kaxiras, Ab initio tight-binding Hamiltonian for transition metal dichalcogenides, *Phys. Rev. B* **92**, 205108 (2015).
- [65] H. Feng, C. Liu, S. Zhou, N. Gao, Q. Gao, J. Zhuang, X. Xu, Z. Hu, J. Wang, L. Chen, J. Zhao, S. Dou, and Y. Du, Experimental Realization of Two-Dimensional Buckled Lieb Lattice, *Nano Lett.* **20**, 2537 (2020).
- [66] O. Samy, S. Zeng, M. D. Birowosuto, and A. El Moutaouakil, A Review on MoS₂ Properties, Synthesis, Sensing Applications and Challenges, *Crystals* **11**, 355 (2021).
- [67] Y. Zhang, R. Zhang, Y. Guo, Y. Li, and K. Li, A review on MoS₂ structure, preparation, energy storage applications and challenges, *J. Alloy. Compd.* **998**, 174916 (2024).
- [68] G.-B. Liu, W.-Y. Shan, Y. Yao, W. Yao, and D. Xiao, Three-band tight-binding model for monolayers of group-VIB transition metal dichalcogenides, *Phys. Rev. B* **88**, 085433 (2013).
- [69] R. Yan, G. Khalsa, B. T. Schaefer, A. Jarjour, S. Rouvimov, K. C. Nowack, H. G. Xing, and D. Jena, Thickness dependence of superconductivity in ultrathin NbS₂, *Appl. Phys. Express* **12**, 023008 (2019).
- [70] J. Chen, Z. Ma, D. Wang, X. Li, S. Li, and B. Bian, Electrical contact between 2D material NbS₂ and WSe₂, *Physica E* **168**, 116179 (2025).
- [71] W.-J. Yin, H.-J. Tan, P.-J. Ding, B. Wen, X.-B. Li, G. Teobaldi, and L.-M. Liu, Recent advances in low-dimensional Janus materials: theoretical and simulation perspectives, *Mater. Adv.* **2**, 7543 (2021).
- [72] R. Li, Y. Cheng, and W. Huang, Recent Progress of Janus 2D Transition Metal Chalcogenides: From Theory to Experiments, *Small* **14**, 1802091 (2018).
- [73] A.-Y. Lu, H. Zhu, J. Xiao, C.-P. Chuu, Y. Han, M.-H. Chiu, C.-C. Cheng, C.-W. Yang, K.-H. Wei, Y. Yang, Y. Wang, D. Sokaras, D. Nordlund, P. Yang, D. Muller, M.-Y. Chou, X. Zhang, and L.-J. Li, Janus monolayers of transition metal dichalcogenides, *Nat. Nanotechnol.* **12**, 744 (2017).
- [74] P. Giannozzi, O. Andreussi, T. Brumme, O. Bunau, M. Buongiorno Nardelli, M. Calandra, R. Car, C. Cavazzoni, D. Ceresoli, M. Cococcioni, N. Colonna, I. Carnimeo, A. Dal Corso, S. de Gironcoli, P. Delugas, R. A. DiStasio, A. Ferretti, A. Floris, G. Fratesi, G. Fugallo, R. Gebauer, U. Gerstmann, F. Giustino, T. Gorni, J. Jia, M. Kawamura, H.-Y. Ko, A. Kokalj, E. Küçükbenli, M. Lazzeri, M. Marsili, N. Marzari, F. Mauri, N. L. Nguyen, H.-V. Nguyen, A. Otero-de-la Roza, L. Paulatto, S. Poncè, D. Rocca, R. Sabatini, B. Santra, M. Schlipf, A. P. Seitsonen, A. Smogunov, I. Timrov, T. Thonhauser, P. Umari, N. Vast, X. Wu, and S. Baroni, Advanced capabilities for materials modelling with Quantum ESPRESSO, *J. Phys.: Condens. Matter* **29**, 465901 (2017).
- [75] Y. C. Cheng, Z. Y. Zhu, M. Tahir, and U. Schwingenschlögl, Spin-orbit-induced spin splittings in polar transition metal dichalcogenide monolayers, *Europhys. Lett.* **102**, 57001 (2013).
- [76] A. A. Mostofi, J. R. Yates, Y.-S. Lee, I. Souza, D. Vanderbilt, and N. Marzari, wannier90: A tool for obtaining maximally-localised Wannier functions, *Comput. Phys. Commun.* **178**, 685 (2008).
- [77] G. Pizzi, V. Vitale, R. Arita, S. Blügel, F. Freimuth, G. Géranton, M. Gibertini, D. Gresch, C. Johnson, T. Koretsune, J. Ibañez-Azpiroz, H. Lee, J.-M. Lihm, D. Marchand, A. Marrazzo, Y. Mokrousov, J. I. Mustafa, Y. Nohara, Y. Nomura, L. Paulatto, S. Poncè, T. Ponweiser, J. Qiao, F. Thöle, S. S. Tsirkin, M. Wierzbowska, N. Marzari, D. Vanderbilt, I. Souza, A. A. Mostofi, and J. R. Yates, Wannier90 as a community code: new features and applications, *J. Phys.: Condens. Matter* **32**, 165902 (2020).
- [78] D. K. Wilson and G. Feher, Electron Spin Resonance Experiments on Donors in Silicon. III. Investigation of Excited States by the Application of Uniaxial Stress and Their Importance in Relaxation Processes, *Phys. Rev.* **124**, 1068 (1961).
- [79] T. Thonhauser, D. Ceresoli, D. Vanderbilt, and R. Resta, Orbital Magnetization in Periodic Insulators, *Phys. Rev. Lett.* **95**, 137205 (2005).
- [80] D. Xiao, J. Shi, and Q. Niu, Berry Phase Correction to Electron Density of States in Solids, *Phys. Rev. Lett.* **95**, 137204 (2005).
- [81] J. Shi, G. Vignale, D. Xiao, and Q. Niu, Quantum Theory of Orbital Magnetization and Its Generalization to Interacting Systems, *Phys. Rev. Lett.* **99**, 197202 (2007).
- [82] D. Xiao, M.-C. Chang, and Q. Niu, Berry phase effects on electronic properties, *Rev. Mod. Phys.* **82**, 1959 (2010).
- [83] J. Fuchs, F. Piéchon, M. Goerbig, and G. Montambaux, Topological Berry phase and semiclassical quantization of cyclotron orbits for two dimensional electrons in coupled band models, *Eur. Phys. J. B* **77**, 351 (2010).
- [84] K. Osumi, T. Zhang, and S. Murakami, Kinetic magnetoelectric effect in topological insulators, *Commun. Phys.* **4**, 211 (2021).
- [85] A. Pezo, D. García Ovalle, and A. Manchon, Orbital Hall effect in crystals: Interatomic versus intra-atomic contributions, *Phys. Rev. B* **106**, 104414 (2022).
- [86] S. Bhowal and G. Vignale, Orbital Hall effect as an alternative to valley Hall effect in gapped graphene, *Phys. Rev. B* **103**, 195309 (2021).
- [87] A. Läuchli, F. Mila, and K. Penc, Quadrupolar Phases of the $S = 1$ Bilinear-Biquadratic Heisenberg Model on the Triangular Lattice, *Phys. Rev. Lett.* **97**, 087205 (2006).
- [88] H. Tsunetsugu and M. Arikawa, Spin Nematic Phase in $S=1$

- Triangular Antiferromagnets, *J. Phys. Soc. Jpn.* **75**, 083701 (2006).
- [89] R. M. Martin, Piezoelectricity, *Phys. Rev. B* **5**, 1607 (1972).
- [90] S. Baroni, S. de Gironcoli, A. Dal Corso, and P. Giannozzi, Phonons and related crystal properties from density-functional perturbation theory, *Rev. Mod. Phys.* **73**, 515 (2001).
- [91] H. Ueda, M. García-Fernández, S. Agrestini, C. Romao, J. van den Brink, N. Spaldin, K.-J. Zhou, and U. Staub, Chiral phonons in quartz probed by X-rays, *Nature* **618**, 946 (2023).
- [92] K. Ohe, H. Shishido, M. Kato, S. Utsumi, H. Matsuura, and Y. Togawa, Chirality-Induced Selectivity of Phonon Angular Momenta in Chiral Quartz Crystals, *Phys. Rev. Lett.* **132**, 056302 (2024).
- [93] H. Kageyama, K. Yoshimura, R. Stern, N. V. Mushnikov, K. Onizuka, M. Kato, K. Kosuge, C. P. Slichter, T. Goto, and Y. Ueda, Exact Dimer Ground State and Quantized Magnetization Plateaus in the Two-Dimensional Spin System $\text{SrCu}_2(\text{BO}_3)_2$, *Phys. Rev. Lett.* **82**, 3168 (1999).
- [94] J. E. Sipe and A. I. Shkrebtii, Second-order optical response in semiconductors, *Phys. Rev. B* **61**, 5337 (2000).
- [95] Parker, Daniel E. and Morimoto, Takahiro and Orenstein, Joseph and Moore, Joel E., Diagrammatic approach to nonlinear optical response with application to Weyl semimetals, *Phys. Rev. B* **99**, 045121 (2019).
- [96] T. Qin, Q. Niu, and J. Shi, Energy Magnetization and the Thermal Hall Effect, *Phys. Rev. Lett.* **107**, 236601 (2011).